

ISAC: Training-Free Instance-to-Semantic Attention Control for Improving Multi-Instance Generation

Sanghyun Jo *

OGQ

Seoul, South Korea

SHJO.APRIL@GMAIL.COM

Wooyeol Lee *

Department of Computer Science and Engineering

Seoul National University

Seoul, South Korea

WOOYEOL0519@SNU.AC.KR

Ziseok Lee *

Department of Biomedical Sciences

Seoul National University

Seoul, South Korea

ZISEOKLEE@SNU.AC.KR

Kyungsu Kim †

School of Transdisciplinary Innovations, Interdisciplinary Program in Artificial Intelligence, Department of Biomedical Sciences

Seoul National University

Seoul, South Korea

KYSKIM@SNU.AC.KR

Abstract

Text-to-image diffusion models have recently become highly capable, yet their behavior in multi-object scenes remains unreliable: models often produce an incorrect number of instances and exhibit semantics leaking across objects. We trace these failures to vague instance boundaries; self-attention already reveals instance layouts early in the denoising process, but existing approaches act only on semantic signals. We introduce **ISAC** (Instance-to-Semantic Attention Control), a training-free, model-agnostic objective that performs hierarchical attention control by first carving out instance layouts from self-attention and then binding semantics to these instances. In Phase 1, ISAC clusters self-attention into the number of instances and repels overlaps, establishing an instance-level structural hierarchy; in Phase 2, it injects these instance cues into cross-attention to obtain instance-aware semantic masks and decomposes mixing semantics by tying attributes within each instance. ISAC yields consistent gains on T2I-CompBench, HRS-Bench, and IntraCompBench, our new benchmark for intra-class compositions where failures are most frequent, with improvements of at least 50% in multi-class accuracy and 7% in multi-instance accuracy on IntraCompBench, without any fine-tuning or external models. Beyond text-to-image setups, ISAC also strengthens layout-to-image controllers under overlapping boxes by refining coarse box layouts into dense instance masks, indicating that hierarchical decoupling of instance formation and semantic assignment is a key principle for robust, controllable multi-object generation. Code will be released upon publication.

Keywords: hierarchical, instance-to-semantic, text-to-image, diffusion, training-free, attention

*. Equal Contribution

†. Corresponding Author

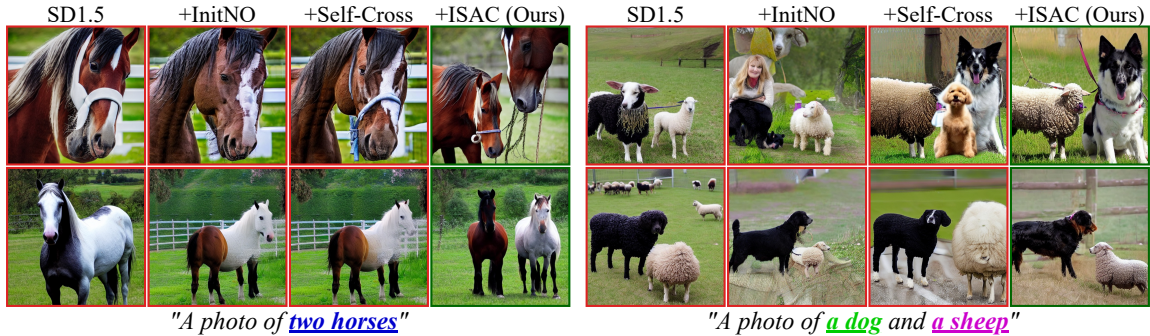


Figure 1. **Importance of instance-level control for multi-object generation.** Existing text-to-image diffusion models (*e.g.*, SD1.5 [1]) and prior training-free guidance methods [2, 3] still suffer from *count failures* (missing or merged instances) and *semantic mixing* (attributes spilling across objects), whereas ISAC’s instance-first design yields the correct number of instances with clearly separated semantics.

1 Introduction

Text-to-image (T2I) diffusion models [1, 4–7] now produce strikingly realistic images from text prompts. Yet in multi-object scenes their reliability drops sharply. They often generate the wrong number of objects, missing or merging instances (*count failures*), and frequently let attributes or appearances leak between objects (*semantic mixing*). These failures are particularly severe when the scene involves similar objects or multiple instances of the same class, which is a common regime for real-world applications.

Figure 1 illustrates these issues for representative text prompts. Recent training-free T2I guidance methods [2, 3, 8–10] try to address such failures by manipulating internal semantic representations, typically cross-attention maps or text embeddings, to separate concepts at the token level. These approaches can amplify underrepresented words and push apart cross-attention maps of different tokens. However, they do not ensure instance discrimination. When several instances share similar semantics, or when different classes fall under a similar textual description, semantic separation alone cannot prevent objects from being counted incorrectly or from borrowing each other’s appearance.

To understand this limitation more concretely, we analyze multi-object generation within a single supercategory, for example multiple animal subclasses, in Fig. 2. We observe that semantic mixing is most prominent between these closely related subclasses. Cross-attention maps, which primarily encode “what” each pixel represents, tend to produce large overlapping blobs that cover several objects simultaneously. In contrast, self-attention maps capture “where” instance structures emerge, and already exhibit instance-like clustering early in the diffusion process [11]. By constructing instance-aware semantic masks using self-attention structure as in Eq. (2), we can clearly see that proper instance separation must precede semantic separation. This analysis suggests that mitigating count failures and semantic mixing requires controlling generation at the instance level first, rather than relying solely on semantic cues.

Motivated by these observations, we introduce **Instance-to-Semantic Attention Control** (ISAC), a hierarchical guidance framework that enforces an instance-first principle. ISAC operates as a two-phase latent optimization objective that decouples count-consistent instance

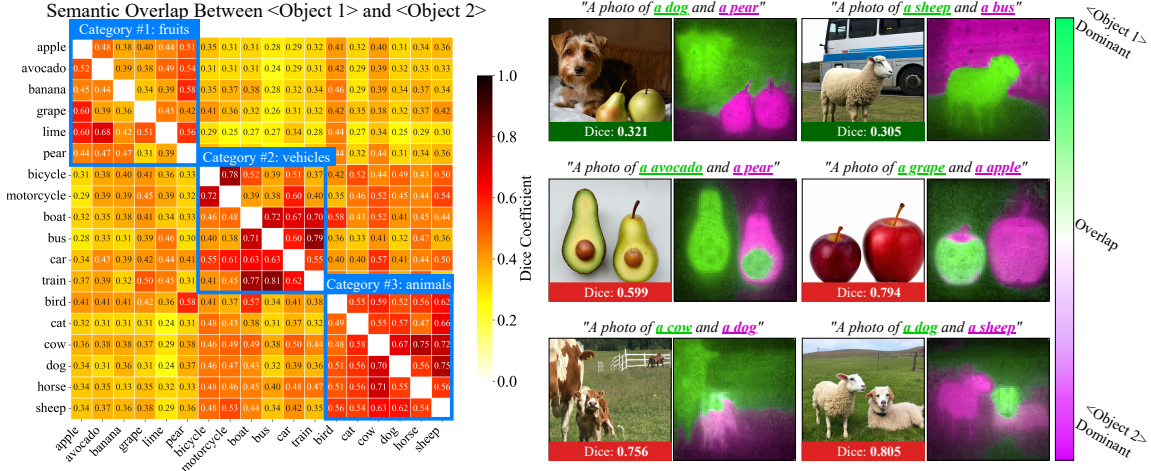


Figure 2. **Semantic overlap across object pairs.** We measure semantic mixing by the Dice coefficient between the two instance-aware semantic masks in Eq. (2) for prompts of the form “A photo of a <object1> and a <object2>” with SD3.5-M [5]. *Left*: heatmap over object pairs. Within-supercategory pairs (fruits, vehicles, animals; blue boxes) show consistently higher overlap, revealing that semantic masks tend to cover multiple similar objects at once. *Right*: qualitative examples. We visualize the signed difference between the two masks, normalized by their summed attention strengths. Color intensity reflects the strength of dominance.

formation from semantic assignment. In Phase 1 (\mathcal{L}_{ins}), ISAC exploits self-attention structure together with instance-count cues to carve out the correct number of disjoint, class-agnostic instance layouts. By repelling overlaps among them, Phase 1 control yields clear instance boundaries. In Phase 2 (\mathcal{L}_{sem}), it injects this instance-stabilized signal into cross-attention to obtain instance-aware semantic masks, then enforces semantic separation across incompatible tokens while binding attributes within each instance. As a result, semantics are aligned per object and do not spill across instances. This two-phase instance-to-semantic control is training-free and model-agnostic, and it improves both text-to-image diffusion [1, 4–7] and layout-to-image diffusion [12] by refining overlapping box layouts into sharp instance masks. To systematically evaluate similar-object regimes under this setting, we further introduce **IntraCompBench**, a new benchmark that focuses on intra-class multi-object compositions.

To summarize, our main contributions are:

- We analyze multi-object scenes in text-to-image diffusion and show that strong overlap of semantic masks within a supercategory, together with a mismatch between self-attention and cross-attention, leads to systematic *count failures* and *semantic mixing*.
- We introduce a hierarchical instance-to-semantic attention control (**ISAC**), a training-free and model-agnostic framework that achieves instance-level control by explicitly separating instance formation (Phase 1: \mathcal{L}_{ins}) from semantic assignment (Phase 2: \mathcal{L}_{sem}).
- We propose **IntraCompBench**, a benchmark that isolates intra-category multi-object compositions to evaluate similar-object failure modes.
- ISAC delivers model-agnostic gains: across three text-to-image benchmarks [13, 14] it improves multi-object metrics by at least 1.9 \times over baseline [1] and consistently boosts performance on five diffusion backbones [4, 5, 12] for both text- and layout-to-image

Table 1. Conceptual comparison with text-to-image methods to improve multi-instance generation.

Method	First preserve instance structure	Separate semantic masks	Applicable to any diffusion models	Require instance counts at inference phase	Require fine-tuning or extra counting models
A&E <small>SIGGRAPH’23 [10]</small>	✗	✓	✓	✗	✗
InitNO <small>CVPR’24 [2]</small>	✗	✓	✓	✗	✗
SynGen <small>NeurIPS’23 [17]</small>	✗	✓	✓	✗	✗
CONFORM <small>CVPR’24 [18]</small>	✗	✓	✓	✗	✗
Self-Cross <small>CVPR’25 [3]</small>	✗	✓	✓	✗	✗
CountGen <small>CVPR’25 [15]</small>	✗	✓	✗	✓	✓
Counting Guidance <small>WACV’25 [16]</small>	✗	✓	✗	✓	✓
ISAC (Ours)	✓	✓	✓	✓	✗

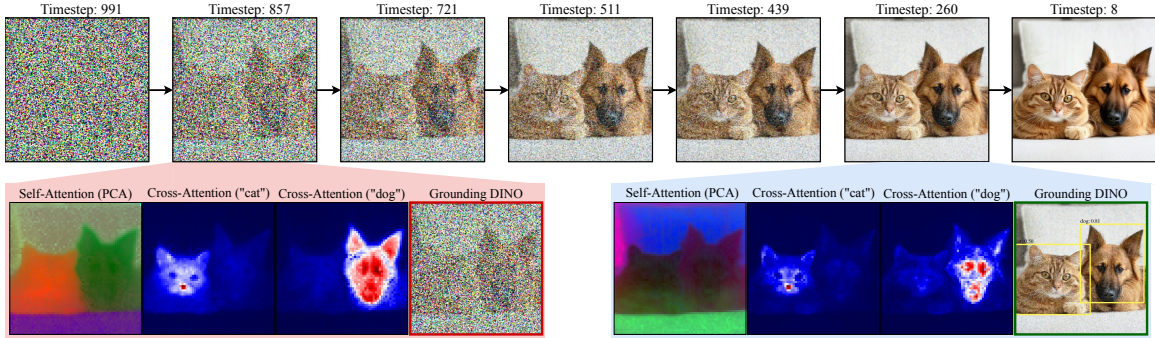


Figure 3. **Dynamics of Text-to-image diffusion models.** In early diffusion steps, instance structures actively emerge while semantics underdeveloped. In later diffusion steps, instance structures are stabilized and semantic refinements happen. As detection models (*e.g.*, [19]) rely on strong semantic cues, they are only effective in later steps. We use a prompt of “A photo of a cat and a dog” on SD3.5-M [5].

generation, while even surpassing prior counting-supervised methods [15, 16] by at least 7% absolute accuracy without any additional training.

2 Related Work

Training-free text-to-image guidance Cross-attention (CA) exposes spatial footprint of textual semantics [20], and many training-free methods leverage this interface. Some steer CA indirectly by mitigating bias in per-instance text embeddings or token organization [8, 9, 21]. Others intervene directly in CA: Attend-and-Excite [10] amplifies attention peaks to recover neglected objects, while SynGen and CONFORM [17, 18] separate and bind CA maps with contrastive objectives and parser-derived relations. Extensions such as InitNO [2] and Self-Cross [3] incorporate structural cues from self-attention (SA), but mainly to form instance-aware semantic masks rather than to establish the instance structure itself. By ignoring instance formation and directly separating semantics spatially, prior approaches often suffer from *count failures* and *semantic mixing*. In contrast, ISAC first establishes the correct number of instance structures and only then binds semantics. This ensures reliable instance discrimination while requiring only minimal instance-count cues (see Tab. 1).

Layout-to-image methods Token-level semantics in text prompts lack instance discriminative cues, making additional layout conditions (*e.g.*, bounding boxes) appealing. Box layouts are lightweight and, combined with the spatial understanding of large language models

(LLMs), support a two-stage pipeline that first generates a bounding-box layout from text and then conditions image synthesis on that layout [22, 23]. While state-of-the-art controllers provide dense layout control [12, 24–28], they often struggle with overlapping layouts [29, 30]. Training-free layout-to-image methods [31–38] help, yet they do not ensure instance discrimination. Constraining attention within each box—by excluding background [37] or other instances’ layouts [38]—only separates semantic regions rather than instance structures. In contrast, ISAC first forms instance structures from internal attention without layout priors, then assigns semantics. This addresses controllers’ failures under overlapping boxes by carving coarse box layouts into dense instance masks.

Count-supervised text-to-image methods Given the limits of box layouts, recent work pursues instance-level control with minimal supervision via instance counts. One approach leverages a pretrained vision model to enforce counts [16], but because such models rely on strong semantic cues, they are ineffective in early diffusion steps when instances form (see Fig. 3). Another replaces boxes with automatically generated dense masks to guide instance separation [15, 39], yet this depends on a fine-tuned mask generator and extensive training to cover broad vocabularies and compositions. In contrast, ISAC is the first training-free method to achieve instance-level control.

Evaluation and benchmarks To evaluate multi-object generation, T2I-CompBench [13] and HRS-Bench [14] are widely adopted. However, they do not isolate intra-category cases where (i) *count failures* and (ii) *semantic mixing* are most prevalent. TIFA [40] and SSD [3] focus on this issue but benchmark only simple 2–3-object compositions, with SSD further limited by a small prompt set (31 two-object and 21 three-object prompts). We address this gap with IntraCompBench, a comprehensive benchmark that stress-tests similar-object generation across 2–5-object compositions with diverse prompt combinations.

3 Method

ISAC targets two core failure modes of multi-object generation, *count failures* and *semantic mixing*, which stem from vague instance boundaries. Guided by evidence that coarse structure emerges before fine-grained semantics in diffusion [20, 41], we design ISAC as a hierarchical, instance-first, training-free guidance. Figure 4 illustrates how Phase 1 (Sec. 3.2) shapes class-agnostic instance layouts from self-attention and how Phase 2 (Sec. 3.3) aligns semantic evidence to these layouts, yielding instance-aware semantics that prevent cross-instance mixing.

3.1 Background

Text-to-image diffusion models Diffusion models learn to reverse a forward noising process that gradually corrupts a sample X_0 into noise X_T , conditioned on a text embedding $\mathcal{T} \in \mathbb{R}^{L \times d}$. At inference time, a neural network ϵ_θ iteratively denoises $X_T \sim \mathcal{N}(0, I)$ to obtain X_0 . In text-to-image models, denoising is typically performed in latent space; a VAE decoder \mathcal{D} then maps X_0 to pixel space, yielding the final image $I_0 = \mathcal{D}(X_0)$. ISAC is model-agnostic: it only requires access to X_t and the model’s attention maps.

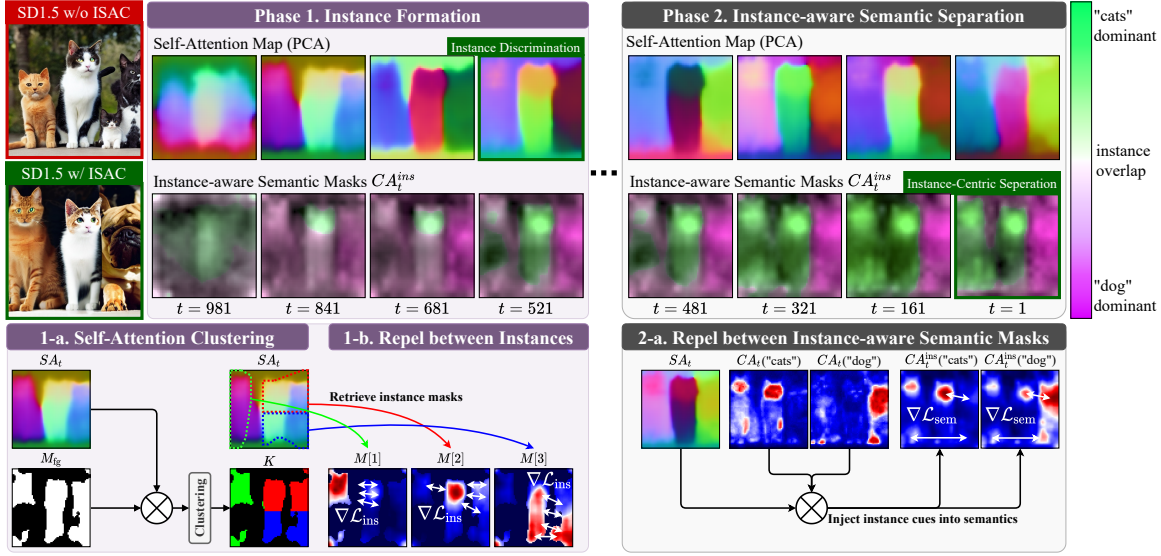


Figure 4. **Overview of ISAC.** Given a multi-object prompt, ISAC steers diffusion in two phases. In Phase 1 (Sec. 3.2), we cluster the self-attention map into N class-agnostic instance masks and apply an instance separation loss that repels overlaps, yielding clean instance layouts early in the trajectory. In Phase 2 (Sec. 3.2), the self-attention map with reliable instance structures is injected into cross-attention (CA) to produce instance-aware semantic masks, and a repel-and-bind loss pushes apart incompatible tokens while binding attributes within each instance so that semantics follow instance shapes. An instance-to-semantics schedule gradually shifts weight from Phase 1 to Phase 2 across timesteps, aligning ISAC’s control with the diffusion dynamics (see Sec. 3.4).

Prompt notation From each prompt we parse class tokens $\{\tau_i\}_{i=1}^k$, per-class instance counts $\{n_i\}_{i=1}^k$, and optional attributes $\{\chi_{i,j}\}$, with total instance count $N = \sum_i n_i$. We use an LLM-based parser to automatically obtain $(\{\tau_i\}, \{n_i\}, \{\chi_{i,j}\})$; additional details and examples are provided in Appendix A.

Attention At each denoising timestep t , the denoiser ϵ_θ uses self-attention (SA) to capture spatial relations within the latent $X_t \in \mathbb{R}^{HW \times d}$ and cross-attention (CA) to align X_t with text embeddings \mathcal{T} . Both compute maps from queries and keys obtained via learned projections (W_Q, W_K) . For SA, $Q_t^{\text{self}} = X_t W_Q^{\text{self}}$ and $K_t^{\text{self}} = X_t W_K^{\text{self}}$. For CA, $Q_t^{\text{cross}} = X_t W_Q^{\text{cross}}$ and $K_t^{\text{cross}} = \mathcal{T} W_K^{\text{cross}}$. For a head of width d_h at layer l , the per-head attention maps are $SA_l^h(X_t) = \text{softmax}(Q_t^{\text{self}} K_t^{\text{self}}^\top / \sqrt{d_h}) \in [0, 1]^{HW \times HW}$, $CA_l^h(X_t, \mathcal{T}) = \text{softmax}(Q_t^{\text{cross}} K_t^{\text{cross}}^\top / \sqrt{d_h}) \in [0, 1]^{HW \times L}$.

We register hooks on all attention layers to read out SA and CA without altering computation. Let M be the number of attention layers and h_l the number of heads at layer l . For each timestep t , we obtain a single SA/CA pair by averaging the attention maps over all layers and heads:

$$SA_t = \frac{1}{N} \sum_{l,h} SA_l^h(X_t), CA_t = \frac{1}{N} \sum_{l,h} CA_l^h(X_t, \mathcal{T}) \quad (1)$$

where $N = \sum_{l=1}^M h_l$. For U-Nets where attention maps vary in spatial resolution, we bilinearly upsample each map to the highest resolution and take the average (See Appendix A).

3.2 Phase 1: Instance Formation

We hypothesize that pixels belonging to the same instance exhibit higher mutual attention, whereas pixels from different instances attend to each other less. This suggests that the N most discriminative pixel clusters reveal N disjoint instance layouts. We translate this property into a guidance objective by (i) clustering self-attention into N groups and (ii) penalizing overlap between the resulting masks. This loss strengthens attention within each instance and suppresses attention outside its boundary.

Self-attention to N clusters Self-attention (SA) encodes instance structure, but also assigns non-trivial mass to background regions, so clustering it over the whole image can split or merge instances. We therefore first build a foreground gate M_{fg} from semantic maps and then cluster SA only within this foreground. Given accumulated maps SA_t and CA_t from Eq. (1), we leverage the instance structure encoded in SA_t to modulate CA_t and form instance-aware semantic masks:

$$CA_t^{\text{ins}} = SA_t CA_t \in [0, 1]^{HW \times L}, \quad (2)$$

where column j highlights the region most responsive to token $\mathcal{T}[j]$. We binarize each column by its mean μ_j and define a foreground gate as the union over class tokens,

$$CA_t^{\text{bin}} \leftarrow \text{Binarize}(CA_t^{\text{ins}}), \quad (3)$$

$$M_{\text{fg}} = \bigcup_{\mathcal{T}[i] \in \{\tau_j\}_{j=1}^k} CA_t^{\text{bin}}[:, i] \in \{0, 1\}^{HW}. \quad (4)$$

Let $\mathcal{I} = \{p : M_{\text{fg}}[p] = 1\}$ and $F := |\mathcal{I}|$. We restrict SA to these foreground positions and cluster its rows into N components (*e.g.*, K-means on SA features, optionally concatenated with normalized coordinates $(x, y) \in [-1, 1]^2$ for spatial coherence). With one-hot assignments $K \in \{0, 1\}^{F \times N}$ (no gradient through K), the resulting instance masks are

$$M = SA_t[\mathcal{I}, \mathcal{I}] \text{stopgrad}(K) \in [0, 1]^{F \times N}. \quad (5)$$

This yields instance masks that highlight pixels attending strongly within the same cluster and weakly outside, leading to sharper instance boundaries. Further details of the instance clustering procedure are provided in Appendix A.

Repel guidance between instance masks From Eq. (5) we obtain instance masks $M[1], \dots, M[N]$ over foreground pixels. To separate instances, we penalize their worst local overlap using the *maximum pixel-wise overlap* (MPO):

$$\text{MPO}(A, B) = \max_{p \in \{1, \dots, F\}} A[p] \cdot B[p], \quad (6)$$

and define the instance separation loss as the maximum MPO over all mask pairs,

$$\mathcal{L}_{\text{ins}}(X_t) = \max_{1 \leq i < j \leq N} \text{MPO}(M[i], M[j]). \quad (7)$$

Within each step we treat K as `stopgrad` and recompute it at the next step, so gradients flow only through SA_t .

Algorithm 1: ISAC with Latent Optimization

Input: Prompt \mathcal{T} , Model ϵ_θ , decoder \mathcal{D} , step size η
Output: Image I_0

- 1 $X_T \sim \mathcal{N}(0, I)$
- 2 **for** $t = T, T-1, \dots, 1$ **do**
- 3 | Call Denoise($X_t, \mathcal{T}, \epsilon_\theta, t$) **with Hooks** $\rightarrow SA_t, CA_t$
- 4 | $CA_t^{\text{ins}} \leftarrow SA_t \cdot CA_t$
- 5 | Build foreground gate and instance masks (Eqs. 3, 4, 5)
- 6 | Compute $\mathcal{L}_{\text{ins}}, \mathcal{L}_{\text{sem}}$ (Eqs. 7, 8)
- 7 | $\mathcal{L}_t(X_t) \leftarrow \lambda_{\text{ins}}(t)\mathcal{L}_{\text{ins}}(X_t) + \lambda_{\text{sem}}(t)\mathcal{L}_{\text{sem}}(X_t)$
- 8 | $\tilde{X}_t \leftarrow X_t - \eta \cdot \nabla_{X_t} \mathcal{L}_t(X_t)$
- 9 | $X_{t-1} \leftarrow \text{Denoise}(\tilde{X}_t, \mathcal{T}, \epsilon_\theta, t)$
- 10 | $I_0 \leftarrow \mathcal{D}(X_0)$ *// Decode to pixel space*

3.3 Phase 2: Instance-aware Semantic Separation

After Phase 1 stabilizes sharp instance boundaries in SA_t , the propagated semantic maps $CA_t^{\text{ins}} = SA_t \cdot CA_t$ in Eq. (2) are activated through spatially partitioned instances. Built on top of this structure, in Phase 2, we apply a repel-and-bind loss \mathcal{L}_{sem} : tokens referring to different instances are pushed apart, while tokens describing the same instance are pulled together, reinforcing clean semantic separation per instance.

Let P_{repel} denote pairs of token indices that should remain distinct (*e.g.*, different classes/instances), and P_{bind} denote pairs that should co-activate (*e.g.*, class/attribute within the same instance). We use MPO as a sharp, local measure of overlap between the corresponding semantic maps:

$$\begin{aligned}\mathcal{L}_{\text{repel}}(X_t) &= \max_{(a,b) \in P_{\text{repel}}} [+ \text{MPO}(CA_t^{\text{ins}}[:, a], CA_t^{\text{ins}}[:, b])] \\ \mathcal{L}_{\text{bind}}(X_t) &= \max_{(a,b) \in P_{\text{bind}}} [1 - \text{MPO}(CA_t^{\text{ins}}[:, a], CA_t^{\text{ins}}[:, b])]\end{aligned}$$

We combine them as a repel-and-bind objective:

$$\mathcal{L}_{\text{sem}}(X_t) = \mathcal{L}_{\text{repel}}(X_t) + \mathcal{L}_{\text{bind}}(X_t) \quad (8)$$

Note that such token relationships are standard in recent methods [17, 18]; our contribution is to bind these relations to the *instance-aware* masks formed in Phase 1 (Sec. 3.2).

3.4 Instance-to-Semantic Loss Schedule

Combining both phases, we define the per-step loss as

$$\mathcal{L}_t(X_t) = \lambda_{\text{ins}}(t) \mathcal{L}_{\text{ins}}(X_t) + \lambda_{\text{sem}}(t) \mathcal{L}_{\text{sem}}(X_t), \quad (9)$$

where $\lambda_{\text{ins}}(t)$ and $\lambda_{\text{sem}}(t)$ control the relative emphasis on instance layout versus semantics over the diffusion trajectory; in practice, we simply set $\lambda_{\text{ins}}(t) = t/T$ and $\lambda_{\text{sem}}(t) = 1 - t/T$ so that early steps focus on instance formation and later steps focus on semantic refinement.

Following prior work [3, 10, 17, 18], we primarily use ISAC for latent optimization as summarized in Algorithm 1. ISAC is also compatible with other guidance schemes, such as latent selection (see Appendix C).

Table 2. Quantitative comparison on HRS-Bench, T2I-CompBench, and IntraCompBench (Multi-Class). Efficiency metrics are the averaged values of #2 to #5 multi-class task of IntraCompBench.

Method	HRSBench (\uparrow)			T2I-CompBench (\uparrow)			IntraCompBench (Multi-Class) (\uparrow)					Efficiency (\downarrow)	
	Color	Spatial	Size	Color	Texture	Complex	#2	#3	#4	#5	Avg.	Latency	VRAM
SD1.5 [1]	0.136	0.094	0.091	0.356	0.406	0.306	28%	2%	1%	0%	8%	8s	4.9 GB
+ A&E SIGGRAPH’23 [10]	0.149	0.104	0.101	0.392	0.447	0.290	48%	10%	5%	2%	16%	17s	9.2 GB
+ SynGen NeurIPS’23 [17]	0.159	0.111	0.107	0.420	0.479	0.311	50%	9%	4%	2%	16%	19s	9.3 GB
+ InitNO CVPR’24 [2]	0.175	0.120	0.116	0.456	0.520	0.338	55%	12%	7%	5%	20%	20s	9.6 GB
+ Self-Cross CVPR’25 [3]	0.170	0.118	0.114	0.445	0.508	0.324	48%	8%	4%	2%	15%	21s	10 GB
+ TEBOpt NeurIPS’24 [9]	0.181	0.127	0.123	0.461	0.544	0.353	52%	11%	8%	3%	18%	17s	9.3 GB
+ ISAC (Ours)	0.318	0.263	0.252	0.683	0.631	0.354	65%	31%	29%	18%	36%	21s	9.7 GB
SD3.5-M [5]	0.425	0.264	0.209	0.796	0.726	0.377	62%	23%	12%	3%	25%	40s	22.9 GB
+ A&E SIGGRAPH’23 [10]	0.427	0.263	0.215	0.798	0.726	0.378	65%	29%	16%	5%	28%	124s	73.8 GB
+ SynGen NeurIPS’23 [17]	0.425	0.260	0.211	0.801	0.718	0.365	66%	28%	15%	6%	28%	131s	74.3 GB
+ InitNO CVPR’24 [2]	0.443	0.275	0.228	0.810	0.728	0.378	77%	31%	17%	7%	33%	138s	74.6 GB
+ Self-Cross CVPR’25 [3]	0.431	0.268	0.219	0.795	0.720	0.371	78%	38%	19%	3%	34%	147s	76.4 GB
+ TEBOpt NeurIPS’24 [9]	0.438	0.279	0.220	0.805	0.730	0.381	78%	31%	19%	8%	34%	139s	74.5 GB
+ ISAC (Ours)	0.473	0.350	0.258	0.838	0.739	0.388	98%	51%	40%	20%	52%	140s	74.8 GB

4 Experiments

4.1 Experimental Setup

Benchmarks We evaluate ISAC on three benchmarks that cover complementary aspects of multi-instance generation: T2I-CompBench [13], HRS-Bench [14], and our IntraCompBench. T2I-CompBench [13] and HRS-Bench [14] are standard for compositional text-to-image evaluation but do not isolate the intra-category regime where *count failures* and *semantic mixing* are most severe, so we introduce IntraCompBench to explicitly target two failure modes: multi-instance accuracy (prompts such as “three dogs”), which asks the model to generate a specified count N of a single class and measures how often the predicted instance count matches N , and multi-class accuracy (prompts such as “a dog, a cat, and a horse”), which asks for one instance of each of k different classes ($N = k$) and measures how often all k classes appear as distinct instances. For both settings, we evaluate generated images using open-vocabulary detection models [19, 42] and a prompt-specific matching procedure between detections and requested classes (see Appendix A for details of our IntraCompBench).

Implementation details We strictly follow the official inference configurations for all diffusion models [1, 4, 5, 7, 43]. ISAC requires a single hyperparameter, $\eta = 0.01$, shared across all models and benchmarks; a sensitivity analysis for η is provided in Appendix A. For each text prompt, we automatically extract class tag–count pairs (τ_i, n_i) and simple token relations (P_{repel} and P_{bind}) using the open-source GPT-OSS [44] to ensure reproducibility. More details (*e.g.*, GPT instructions) are described in Appendix A.

4.2 Comparison with State-of-the-art Approaches

Table 2 summarizes quantitative results for two popular diffusion models [1, 5]. With similar inference cost, ISAC clearly outperforms existing approaches on every metric of HRS-Bench, T2I-CompBench, and the multi-class setting of IntraCompBench. The largest improvements appear in the intra-category regime: on SD1.5 [1], the average multi-class accuracy on IntraCompBench increases from 20% for the strongest baseline [2] to 36% with ISAC, and the HRS-Bench spatial score is roughly doubled (0.127 to 0.263). On the stronger SD3.5-M

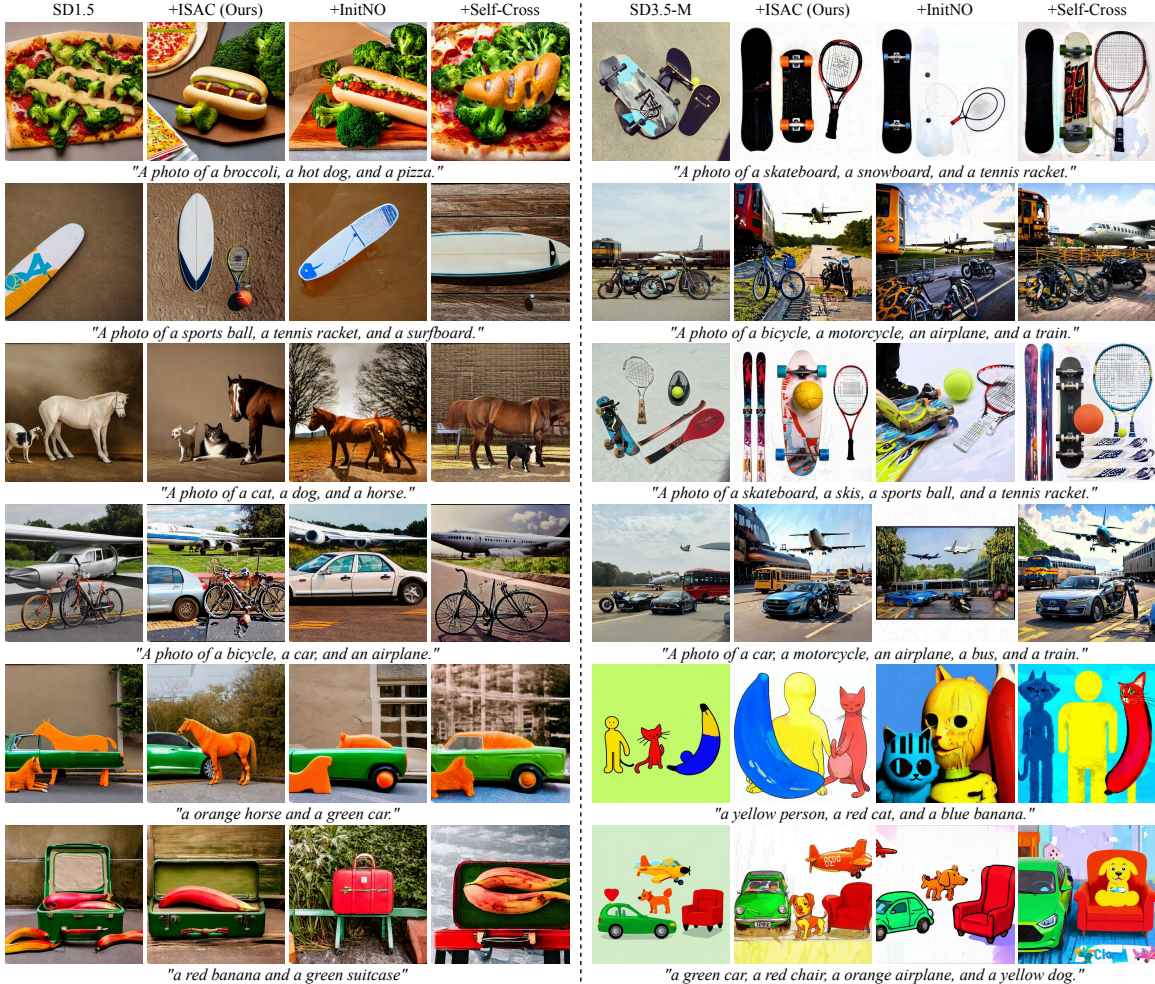


Figure 5. Qualitative comparison using SD1.5 [1] and SD3.5-M [5] as a backbone and added attention control methods.

backbone, ISAC still provides a clear margin with especially large gains in the more crowded #4 and #5 cases. These trends indicate that our instance forming first attention control is most beneficial exactly where multiple similar objects must be separated and counted.

As shown in Fig. 5, previous state-of-the-art methods [2, 3] frequently blur boundaries between objects or merge categories into hybrid shapes when several related objects appear in a scene. By contrast, ISAC allocates distinct, spatially coherent instances to each requested class while maintaining their attributes. This behavior is consistent across prompts (from simple color–shape compositions to scenes with multiple vehicles or animals) and across two diffusion models [1, 5]. Additional quantitative results for more backbones are provided in Appendix G.

4.3 Discussion

ISAC vs. prior count-supervised methods As shown in Tab. 3, ISAC achieves 70% and 76% instance-counting accuracy on SD1.4 [1] and SDXL [4], surpassing count-supervised

Table 3. Comparison with count-supervised methods [15, 16] and ISAC on IntraCompBench.

Method	IntraCompBench (Instance) (\uparrow)					Efficiency (\downarrow)	
	#2	#3	#4	#5	Avg.	Latency	VRAM
SD1.4 [1]	94%	74%	28%	22%	55%	8s	4.9GB
+ CG <small>WACV'25</small> [16]	79%	67%	32%	19%	49%	14s	17.5GB
+ ISAC (Ours)	100%	90%	51%	40%	70%	21s	9.7GB
SDXL [4]	90%	71%	49%	32%	61%	48s	12.8GB
+ CountGen <small>CVPR'25</small> [15]	97%	83%	52%	44%	69%	100s	55.3GB
+ ISAC (Ours)	96%	89%	71%	47%	76%	101s	29.8GB



Figure 6. Qualitative examples on SD1.5 [1] and SD3.5-M [5] where prompts specify exact counts.

methods (49% for Counting Guidance [16] and 69% for CountGen [15]) even though all methods are given the same instance-count supervision and ISAC uses no fine-tuning or extra training data. Counting-based supervision for auxiliary models can only be exploited once semantic evidence is sufficiently clear, so its effect is limited to later diffusion steps and to samples where object categories are already well formed. By contrast, ISAC strengthens instance structure at early timesteps, before semantics have fully emerged, by reshaping attention to separate and stabilize instance-level regions; this enables it to reach the highest counting accuracy without auxiliary networks [45] or extra labels such as instance-level mask annotations.

Flexibility of ISAC Beyond the text-to-image setting in Tab. 2 and Tab. 3, Tab. 4 shows that ISAC also improves layout-to-image controllers [12]. On HRS-Bench, ISAC yields the largest gains among layout refinements [37]. This advantage comes from enforcing instance separation for adjacent boxes early in the diffusion trajectory, rather than only constraining attention within each box. By carving out dense instance masks from initial coarse box layouts, ISAC prevents neighboring objects from being merged and delivers more reliable counting in crowded layouts in Fig. 7.

Table 4. Effect of ISAC for the layout-to-image setup.

Method	HRSBench (\uparrow)			
	Counting (F1)	Color (Acc.)	Spatial (Acc.)	Size (Acc.)
GLIGEN [12]	66.58	30.74	26.75	18.78
+ CAR&SAR [37]	67.54	40.22	27.74	26.32
+ ISAC (Ours)	71.28	45.21	28.12	27.51

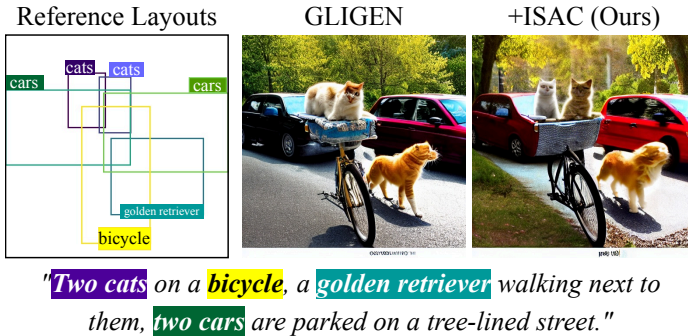


Figure 7. Example of applying ISAC to layout-to-image generation.

Importance of instance-to-semantic schedule Table 5 shows that both losses and their ordering are critical. Optimizing only the instance term (A) yields strong multi-instance accuracy but almost no gain on multi-class prompts, indicating that it can form the right number of structures but cannot reliably assign semantics. Using only the semantic term or a fixed balance (B–C) is also suboptimal, since semantic separation without prior boundary stabilization is unstable. The reverse schedule that goes from semantic to instance (D) further degrades multi-class accuracy. Our instance-to-semantic schedule (E) achieves the best performance on both metrics, supporting the hypothesis that instance structure should be established first and then refined semantically.

Table 5. Effect of ISAC loss schedule. “Class” and “Instance” are multi-class and multi-instance accuracy, respectively.

	Description	$\lambda_{\text{ins}}(t)$	$\lambda_{\text{sem}}(t)$	Class	Instance
A	Instance Only	1	0	10%	65%
B	Semantic Only	0	1	28%	54%
C	Fixed Balance	0.5	0.5	25%	60%
D	Semantic-to-Instance	$1 - t/T$	t/T	21%	55%
E	Instance-to-Semantic	t/T	$1 - t/T$	36%	69%

Effect of MPO Table 6 evaluates alternative similarity metrics in place of MPO. Replacing MPO with MAE, KL, or IoU consistently degrades performance, reducing multi-class accuracy from 36% to at most 20% and multi-instance accuracy from 69% to at most 61%. This gap indicates that MPO’s margin-based separation between class-specific masks is better suited to enforcing instance-aware semantic decoupling than generic overlap measures.

Table 6. Analysis of alternative similarity metrics in Eq. 6.

Method	Metric	IntraCompBench (\uparrow)	
		Multi-Class	Multi-Instance
SD1.5 [1]	N/A	8%	54%
+ ISAC	MAE	9% <i>(+1%)</i>	55% <i>(+1%)</i>
+ ISAC	KL	16% <i>(+8%)</i>	60% <i>(+6%)</i>
+ ISAC	IoU	20% <i>(+12%)</i>	61% <i>(+7%)</i>
+ ISAC	MPO	36% <i>(+28%)</i>	69% <i>(+15%)</i>

5 Conclusion

In this work, we analyze multi-object image synthesis through the lens of internal instance structure and semantics, showing that their mismatch in diffusion models leads to instance count failures and semantic mixing. Building on this diagnosis, we propose ISAC that introduces hierarchical attention control by first forming clear instance structures and then assigning semantics across these stabilized instances. ISAC consistently improves text- and layout-to-image generation across three benchmarks and five diffusion backbones, and our IntraCompBench further demonstrates that ISAC substantially strengthens multi-object composition and even surpasses prior count-supervised methods. Taken together, these findings indicate that instance-first dynamics offer a robust principle for controllable multi-object generation and suggest a promising path toward extending decoupled structural and semantic control to video, 3D content, medical imaging, and other structured generative settings.

Acknowledgments and Disclosure of Funding

This work was supported by the Institute of Information & Communications Technology Planning & Evaluation (IITP) grant funded by the Korea government (MSIT) [RS-2025-02305581], [RS-2025-25442338 (AI Star Fellowship Support Program at SNU)], and [RS-2021-II211343 (Artificial Intelligence Graduate School Program at SNU)]. This work was supported by a grant from the Korea Health Technology R&D Project through the Korea Health Industry Development Institute (KHIDI), funded by the Ministry of Health & Welfare, Republic of Korea [RS-2025-02307233]. This work was supported by the Korea Bio Data Station (K-BDS) with computing resources including technical support. Kyungsu Kim is affiliated with School of Transdisciplinary Innovations, Department of Biomedical Science, Interdisciplinary Program in Artificial Intelligence, Interdisciplinary Program in Bioengineering, Interdisciplinary Program in Bioinformatics, Department of Transdisciplinary Medicine (at SNUH), Medical Research Center, Artificial Intelligence Institute, Seoul National University, Seoul, Republic of Korea.

Appendix A. Implementation Details

A.1 Method Details

Attention accumulation We accumulate self- and cross-attention maps from all attention layers. When self-attention (SA) and cross-attention (CA) maps have different spatial resolutions across layers, in case of U-Net [46] architectures, we bilinearly upsample each map to the highest spatial resolution ($H \times W$) and average over layers and heads to obtain a single SA/CA pair *per step*:

$$SA_t = \frac{1}{\mathcal{N}} \sum_{l=1}^M \sum_{h=1}^{h_l} \text{Upsample}(SA_l^h(X_t), \delta_l) \quad (10)$$

$$CA_t = \frac{1}{\mathcal{N}} \sum_{l=1}^M \sum_{h=1}^{h_l} \text{Upsample}(CA_l^h(X_t, \mathcal{T}), \delta_l) \quad (11)$$

where $\delta_l = H/H_l = W/W_l$ is the upsampling factor for layer l , and $\mathcal{N} = \sum_{l=1}^M h_l$ is the total number of heads.

Then, we apply `min-max` normalization to the accumulated maps as defined in Eq. (13). For a fair comparison, we use the same attention accumulation scheme across all baseline methods [1, 4–7, 43, 47].

Choice of the step size η We evaluate the sensitivity of ISAC to the gradient step size η in Algorithm 1 under our instance-to-semantic schedule. When η is too small, the optimization loss barely decreases and has negligible impact on the generated images. In contrast, excessively large values of η cause latent collapse and noticeably degrade image quality. This trade-off is consistent with other latent-optimization methods [10], and ISAC is subject to the same limitation.

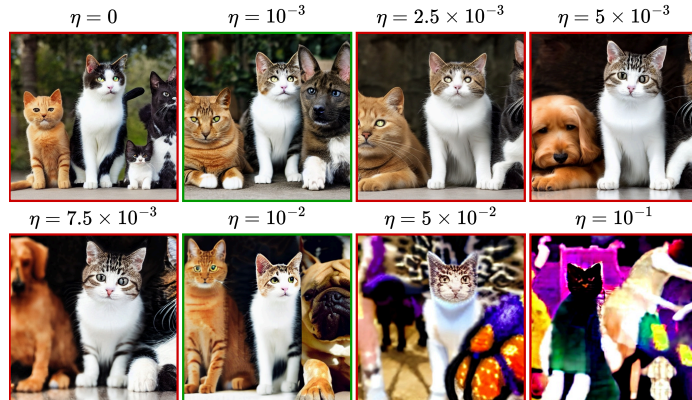


Figure 8. Qualitative comparison of ISAC with various step sizes η . For all cases, we provide “*A photo of two cats and a dog*” as the input prompt and use SD1.5 [1] as the baseline diffusion model.

Empirically, we find that a step size of $\eta = 10^{-2}$ achieves stable improvement without visible artifacts across backbones and datasets (Fig. 8). The gradient-descent update $\tilde{X}_t \leftarrow X_t - \eta \nabla_{X_t} \mathcal{L}_t(X_t)$ in Algorithm 1 is applied once per diffusion timestep, and η is the

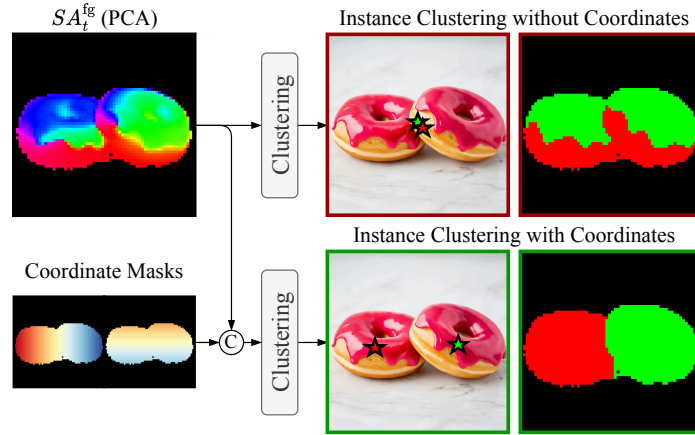


Figure 9. Concatenating normalized coordinates $(x, y) \in [-1, 1]^2$ to SA features stabilizes clustering, reducing erroneous merges and ignorance on hidden boundary signals. The image is generated with the prompt, “*a photo of two donuts*” on SD3.5-M [5]. We averaged all accumulated self/cross-attention maps over timesteps into a single (SA, CA) pair. Then, clustering algorithms are applied to those maps with or without concatenation of spatial coordinates. Note that this is commonly used in previous literature [48–50].

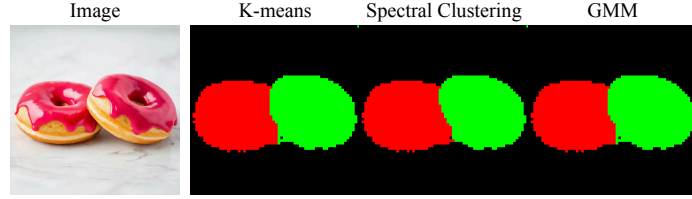


Figure 10. Qualitative comparison of clustering algorithms. The image is generated with the prompt, “*a photo of two donuts*”. We averaged all accumulated self/cross-attention maps over timesteps into a single (SA, CA) pair. Then, clustering algorithms are applied to those maps with concatenation of spatial coordinates. This is an extension of Fig. 9.

Table 7. Comparison of clustering algorithms in terms of accuracy (%) and latency (ms). Latency is defined as the execution time for a one-time application of each clustering algorithm to a self-attention map. This table can be seen as an extension of Tab. 5.

Clustering Algorithm	Multi-Class	Multi-Instance	Latency (ms)
K-means	36%	69%	505 ms
Spectral Clustering	35%	69%	1,630 ms
GMM	36%	69%	8,313 ms

only additional hyperparameter introduced by ISAC; all other settings follow the default configuration of each backbone.

Details of clustering with coordinates We visualize how and why normalized coordinates $(x, y) \in [-1, 1]^2$ are concatenated to the feature vectors in Eq. (5). When adjacent instances are highly semantically similar, their tokens can receive similarly high attention scores, and weak boundary cues are easily overwhelmed (Fig. 9, top/red). By forming a joint space of semantic features and spatial coordinates and performing clustering in this

You are an information-extraction model.

TASK
- Read the given natural-language image prompt and extract a minimal set of objects with their attributes and counts.

OUTPUT FORMAT (must be STRICT JSON, no prose, no code fences)
- An array of items.
- Each item has exactly these keys:
- "object": string, a singular common noun (e.g., "cat", "dog", "car"), lowercase
- "attributes": array of lowercase strings (adjectives/colors/materials/states). Use [] if none.
- "count": integer ≥ 0 . Default to 1 if the text implies a single instance (e.g., "a", "an", "one"). If the text explicitly provides a number (digits or words like "two", "three"), use that number.
- Do NOT include any extra keys or text.
- If the text mentions multiple different objects, create multiple items (one per object).

RULES
- Keep nouns singular in "object" (e.g., "cats" \rightarrow "cat").
- Put descriptive adjectives only in "attributes" (e.g., "red", "small", "wooden", "sleeping").
- If attributes are not clearly stated, use an empty list [].
- Ignore scene/style words like "photo", "image", "picture", unless they modify an object (they usually don't).
- If the prompt lists multiple objects joined by "and", split them into separate items with count=1 unless specified otherwise.

EXAMPLES
INPUT: "A photo of a red cat and a dog"
OUTPUT: [{"object": "cat", "attributes": ["red"], "count": 1}, {"object": "dog", "attributes": [], "count": 1}]

INPUT: "three blue cars and a small bus"
OUTPUT: [{"object": "car", "attributes": ["blue"], "count": 3}, {"object": "bus", "attributes": ["small"], "count": 1}]

INPUT: "two large brown bears, one sleeping"
OUTPUT: [{"object": "bear", "attributes": ["large", "brown"], "count": 2}, {"object": "bear", "attributes": ["sleeping"], "count": 1}]

NOW EXTRACT FROM THIS TEXT
"prompt"

(a) LLM instruction for prompt parsing

Prompt: "two chickens, four pens and one lemon"
Output: [{"object": "chicken", "attributes": [], "count": 2}, {"object": "pen", "attributes": [], "count": 4}, {"object": "lemon", "attributes": [], "count": 1}]

Prompt: "two people are sitting in a coffee shop, both using their cell phones to text and check emails."
Output: [{"object": "person", "attributes": [], "count": 2}, {"object": "cell phone", "attributes": [], "count": 2}]

Prompt: "a green car, a red chair, a orange airplane and a yellow dog."
Output: [{"object": "car", "attributes": ["green"], "count": 1}, {"object": "chair", "attributes": ["red"], "count": 1}, {"object": "airplane", "attributes": ["orange"], "count": 1}, {"object": "dog", "attributes": ["yellow"], "count": 1}]

Prompt: "The fluffy pillow and glass lampshade rest on the wooden nightstand by the metallic bed."
Output: [{"object": "pillow", "attributes": ["fluffy"], "count": 1}, {"object": "nightstand", "attributes": ["wooden"], "count": 1}, {"object": "lampshade", "attributes": ["glass"], "count": 1}, {"object": "bed", "attributes": ["metallic"], "count": 1}]

Prompt: "The sharp, steel **blades** of the chef's knives sliced through the fresh, juicy **vegetables** with ease, creating a colorful medley of flavors and textures."
Output: [{"object": "blade", "attributes": ["sharp", "steel"], "count": 1}, {"object": "vegetable", "attributes": ["fresh", "juicy"], "count": 1}]

Prompt: "one cake sits on a white plate in the middle of a kitchen counter, surrounded by colorful sprinkles, a single lit birthday candle, and **a few** pieces of confetti."
Output: [{"object": "cake", "attributes": [], "count": 1}, {"object": "plate", "attributes": ["white"], "count": 1}, {"object": "sprinkle", "attributes": ["colorful"], "count": 1}, {"object": "candle", "attributes": ["lit", "birthday"], "count": 1}, {"object": "confetti", "attributes": [], "count": 1}]

Prompt: "a black, mechanical keyboard sits on a white desk, illuminated by a bright lamp and surrounded by **a few** books and papers."
Output: [{"object": "keyboard", "attributes": ["black", "mechanical"], "count": 1}, {"object": "desk", "attributes": ["white"], "count": 1}, {"object": "lamp", "attributes": ["bright"], "count": 1}, {"object": "book", "attributes": [], "count": 1}, {"object": "paper", "attributes": [], "count": 1}]

(b) Prompt parsing examples

Figure 11. Details on LLM-guided automatic prompt parsing.

augmented space, the clustering better respects spatial connectivity within each instance, making boundaries more separable and amplifying otherwise hidden boundary signals (Fig. 9, bottom/green).

Choice of clustering algorithm We compare alternative clustering algorithms in Tab. 7 and Fig. 10. While K-means, spectral clustering, and Gaussian mixture models (GMMs) achieve similar performance on both *Multi-Class* and *Multi-Instance* accuracy, K-means, which we adopt as our default choice, is approximately $3\times$ to $16\times$ faster. Given this favorable speed–accuracy trade-off, we use K-means for ISAC.

Automatic prompt parsing We use an LLM-based parser to automatically extract class tokens τ_i , counts n_i , attributes $\{\chi_{i,j}\}$, and token relations for P_{repel} and P_{bind} from natural-language prompts. Figure 11(a) shows the instruction used for this parsing procedure and Figure 11(b) provides example outputs on prompts from T2I-CompBench and HRS-Bench. In all experiments, we use GPT-OSS-20B [44], which produces reliable and consistent parses in practice. For a moderately complex prompt such as *"The fluffy pillow and glass lampshade rest on the wooden nightstand by the metallic bed."*, a single forward pass of the parser takes about 10 seconds and requires roughly 40 GB of VRAM on a single A100 GPU.

While the LLM parser produces highly accurate outputs overall, our current rules do not resolve ambiguous count expressions such as "a few", "several", "a couple of", or plurals without explicit numerals (e.g., "blades"). Handling these ambiguous counts is beyond the scope of

our experiments, but it could be addressed by sampling counts from a small candidate set, for example $\mathcal{N} = \{3, 4\}$, or by providing targeted few-shot examples to the LLM.

Cross-attention normalization Baseline methods, Attend-and-Excite [10], InitNO [2], and TEOpt [9], utilize the the `softmax` normalization technique on cross-attention maps. It operates by applying the `softmax` function to the cross-attention maps along the token dimension, excluding the SOT token at index 0. This sharpens the attention, emphasizing foreground objects while suppressing background noise. The formulation is given by:

$$CA_t^{\text{softmax}} = \text{softmax}(\beta \cdot CA_t[1 :]). \quad (12)$$

Following the official implementation, we set $\beta = 100$ for SD1.4, SD1.5, SD2.1 [1] and SD3.5-M [5] across baseline methods through our experiments (see Secs. 4.2 and F). In contrast, ISAC adopts a simple element-wise `min-max` normalization to rescale attention maps:

$$CA_t^{\text{minmax}} = \frac{CA_t - \min(CA_t)}{\max(CA_t) - \min(CA_t)}. \quad (13)$$

Although both `softmax` and `min-max` normalization are common, we opt for the `min-max` approach due to its practicality as a parameter-free method.

A.2 IntraCompBench Details

Standard benchmarks like T2I-CompBench [13], HRS-Bench [14] and MultiGen benchmark [51] do not isolate the *intra-category* setting where failure on instance discrimination becomes most severe. IntraCompBench is designed to stress this regime and to separately probe the two symptoms we target: (1) *count failures* and (2) *semantic mixing*.

Task 1 – multi-instance accuracy (%) This task isolates count failures. We sample a single class A from a super-category in Tab. 8 and specify an integer $n \in \{2, 3, 4, 5\}$. Now the prompt is formatted as “A photo of [n] [class A]s” (e.g., “A photo of five cats”). Success requires producing exactly $N = n$ instances of A . This primarily evaluates instance formation.

Task 2 – multi-class accuracy (%) This task stresses semantic mixing. We sample $k \in \{2, 3, 4, 5\}$ distinct classes within the same super-category and format into “A photo of a [class A], a [class B], ..., and a [class E]” (e.g., “A photo of a dog, a cat, a horse, a cow, and a sheep”). Success requires (i) forming $N=k$ instances and (ii) assigning the correct semantics to each layout (preventing cross-object leakage). The intra-category constraint makes this substantially harder than prior multi-class settings (e.g., MultiGen [51]), where inter-category separability reduces confusion (see Fig. 2).

Class distribution For reliable automatic evaluation we use a subset of countable object classes from the 80 COCO categories ¹ [52], grouped into four super-categories: animals, vehicles, sports, and food (Tab. 8). We exclude classes such as “*person*”, very small objects

1. Most detection models are trained on COCO classes, so we focus our evaluation on COCO, where the pretrained models are most reliable, rather than experimenting with new classes from datasets like ADE. In practice, MultiGen results in TokenCompose [51] have shown minimal differences in performance trends between COCO and ADE.

Table 8. Countable classes from COCO [52] dataset used in the evaluation.

Category	Classes
Animal	(9 classes) cat, dog, horse, sheep, cow, elephant, bear, zebra, giraffe
Vehicle	(8 classes) bicycle, car, motorcycle, airplane, bus, train, truck, boat
Sports	(10 classes) skateboard, snowboard, skis, sports ball, baseball bat, baseball glove, tennis racket, surfboard, kite, frisbee
Food	(10 classes) banana, apple, sandwich, orange, broccoli, carrot, hot dog, pizza, donut, cake

(*e.g.*, “*fork*”), ambiguous items (*e.g.*, “*book*”), or objects whose duplication is ill-defined (*e.g.*, “*bench*”), due to difficulties in reliable detection or instance differentiation.

Evaluation via ensemble To evaluate accuracy, we use an ensemble of three detectors: Grounding DINO [19], YOLOE [42], and YOLOv12 [53]. And adopt a 2-of-3 agreement rule, in other words, an instance is considered correctly detected only if captured by at least two detectors. Accuracy is the ratio of correctly detected instances to the target number of instances (k for multi-class, n for multi-instance). For example, if “cat” and “dog” are detected in the image from the text prompt “A photo of a cat, a dog, a horse, a cow and a sheep”, then the accuracy is calculated as $2/5 = 40\%$ for multi-class accuracy. For multi-instance accuracy, if 3 instances of “cat” are detected in the image from the text prompt “A photo of five cats”, then the accuracy is calculated as $3/5 = 60\%$.

Table 9. Possible combinations of classes for multi-class evaluation.

Category	#2	#3	#4	#5
Animal (9 classes)	36	84	126	126
Vehicle (8 classes)	28	56	70	56
Sports (10 classes)	45	120	210	252
Food (10 classes)	45	120	210	252
Total	154	380	616	686

Prompt sampling For multi-class evaluation, we sample 20% of all combinations in Tab. 9 for each $k \in \{2, 3, 4, 5\}$ and generate 10 images per prompt. For example, in #5-class evaluation, we randomly sample 25 animal, 11 vehicle, 50 sports, 50 food combinations; 136 prompts total. For multi-instance evaluation, we generate 10 images for each class in the four super-categories for every $n \in \{2, 3, 4, 5\}$, yielding 37 unique prompts per n .

A.3 Evaluation Details

For the layout-to-image evaluation in Tab. 4 and Fig. 7, we use HRS-Bench [14] and follow the two-stage pipeline established by prior work [37]: (i) generate text-to-box layouts with an LLM, then (ii) synthesize images conditioned on those layouts. To ensure comparability, we directly reuse the LLM-produced box layouts released in Attention-Refocusing [37] and run only the layout-conditioned image generation step.

Although OverLayBench [29] is tailored for evaluating overlapping layouts, its publicly available annotations are not directly compatible with training-free layout-to-image guidance

methods [33–38]. OverLayBench provides a global prompt together with (local prompt, bounding box) pairs, where each local prompt specifies the semantics within its box. Training-based controllers [12, 24–28] can ingest an *arbitrary* local prompt via dedicated layout adapters. In contrast, existing training-free layout-to-image guidance methods [33–38] require per-layout class tokens $\{\tau_i\}$ to be present in the *global* prompt. Because this condition is not guaranteed in the public OverLayBench data, it precludes a fair comparison with ISAC. We leave a comprehensive quantitative study on OverLayBench—after reconciling prompt formats—to future work.

Appendix B. Broader Related Work Comparisons

S-CFG [54] highlights spatial inconsistencies in global Classifier-Free Guidance (CFG) [55] and proposes region-level guidance that leverages self- and cross-attention maps. However, S-CFG primarily *amplifies* semantic evidence within semantically segmented patches. It neither disentangles competing semantic signals nor establishes instance boundaries from structural cues.

Beyond Counting Guidance [16], several works [56, 57] steer generation by querying pretrained vision models as external perceptual signals. Dense Geometry Alignment [56] aligns segmentation masks predicted from intermediate images with the target object layouts. Yet, because these vision models [19] are trained on clean, semantically rich images, their predictions on noisy diffusion states are unreliable, yielding weak guidance (see Fig. 3). Moreover, many approaches apply predictions on Tweedie-denoised intermediates [58]; Tweedie’s correction is not applicable to flow-matching models [59] such as SD3.5-M [5], limiting the practicality of using external models in this regime.

Specifically, CountGen [15] is a two-stage approach that first establishes instance-mask layouts with a fine-tuned `ReLayout` module and then applies guidance conditioned on the resulting masks. We find its gains stem largely from the quality of the mask proposals; without explicit instance-separation guidance, it lags behind ISAC on our intra-category settings. ISAC also complements CountGen: replacing CountGen’s guidance with ISAC further improves accuracy, indicating that ISAC’s instance discrimination and CountGen’s mask proposals address different parts of the problem (see Tab. 10).

Table 10. Extended results for CountGen [15] and ISAC.

Method	IntraCompBench (Instance) (↑)				
	#2	#3	#4	#5	Avg.
SDXL [4]	90%	71%	49%	32%	61%
+ CountGen CVPR’25 [15]	97%	83%	52%	44%	69%
+ ISAC (Ours)	96%	89%	71%	47%	76%
+ CountGen + ISAC (Ours)	98%	91%	74%	50%	78%

Among training-free layout guidance methods [22, 31–36, 38, 60], Bounded Attention [38] is the only approach that explicitly separates self- and cross-attention across box-level masks to mitigate semantic mixing. Because it only partitions semantics by boxes, it cannot guarantee instance discrimination and often fails to count correctly in crowded scenes (see Fig. 12).

Moreover, its mutual-exclusivity assumption—each pixel belongs to at most one box—breaks under overlapping or tightly packed layouts. Thus, the resulting suppression of

attention in shared regions degrades spatial control and semantic fidelity (Fig. 13). Since performance can also depend on the arbitrary ownership order under overlap, we exclude Bounded Attention from our layout comparisons.

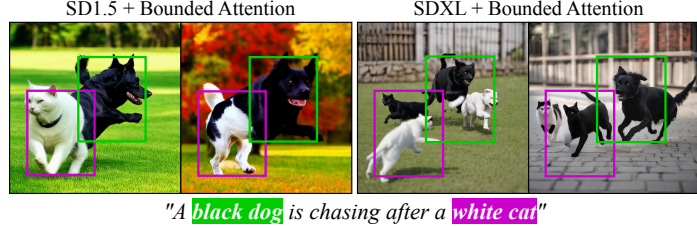


Figure 12. Semantic separation of layout guidance methods (e.g., Bounded Attention [38]) do not ensure instance discrimination.

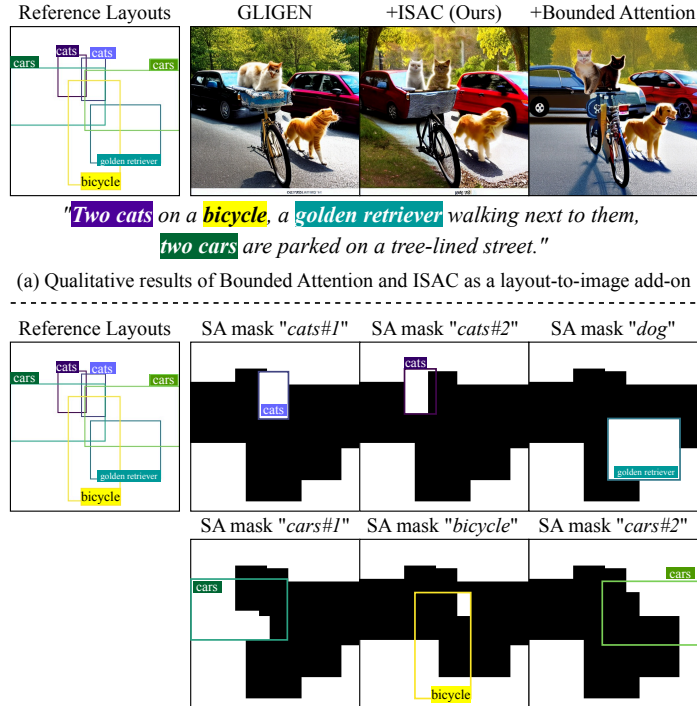


Figure 13. **Limitation of Bounded Attention Masking.** Bounded Attention [38] enforces exclusive pixel ownership among bounding boxes on self-attention maps. Each box can only attend to its owned pixels and the background. We adopt a “smaller-box-first” ownership rule to build self-attention masks. Each mask visualizes pixels attendable from the corresponding layout. As shown, exclusivity suppresses attention in shared regions and degrades control.

Fine-tuned models Several methods ensure object-level separation in attention maps by adapting the base model with external segmentation signals. TokenCompose [51] and CoMat [61] fine-tune the UNet so that cross-attention aligns with masks predicted by a pretrained model [62]. A key limitation is the reduced effective vocabulary compared with general-purpose diffusion backbones, which restricts applicability. ISAC is complementary to these methods and can be applied at inference time without retraining (Tab. 12).

Appendix C. Additional Discussions

C.1 Scalability via Latent Selection

A known limitation of latent optimization techniques, including ISAC, is the increased VRAM usage due to gradient computation, typically $2\times$ to $3.3\times$ compared to the base model (Tab. 2). This can restrict applicability for very large models like Flux [7] and Qwen-Image [43]. However, ISAC can also be implemented via latent selection (ISAC_{LS}, Algorithm 2), which acts as a verifier without backpropagation. This approach is highly efficient, requires no gradient computation, and allows batch processing. In Tab. 11, we present effectiveness of ISAC_{LS} scoring on multi-object generation task. Figure 14 also qualitatively shows ISAC scoring correctly captures whether instances become missing or being semantically mixed.

Algorithm 2: ISAC with Latent Selection

Input: Prompt \mathcal{T} , Model ϵ_θ , decoder \mathcal{D} , Batch size B
Output: Image I_0

```

1   $X_T^{(i)} \sim \mathcal{N}(0, I)$ ,  $S[i] = 0$ ,  $\forall i = 1, \dots, B$ 
2  for  $i = 1, \dots, B$  do
3    for  $t = T, T-1, \dots, 1$  do
4       $X_{t-1}^{(i)} \leftarrow \text{Denoise}(X_t^{(i)}, \mathcal{T}, \epsilon_\theta, t)$ 
5      with Hooks  $\rightarrow SA_t^{(i)}, CA_t^{(i)}$ 
6       $CA_t^{(i), \text{ins}} \leftarrow SA_t^{(i)} \cdot CA_t^{(i)}$ 
7      Build foreground gate and instance masks (Eqs. 3, 4, 5)
8      Compute  $\mathcal{L}_{\text{ins}}, \mathcal{L}_{\text{sem}}$  (Eqs. 7, 8)
9       $\mathcal{L}_t(X_t^{(i)}) \leftarrow \lambda_{\text{ins}}(t)\mathcal{L}_{\text{ins}}(X_t^{(i)}) + \lambda_{\text{sem}}(t)\mathcal{L}_{\text{sem}}(X_t^{(i)})$ 
10     Score Update:  $S[i] \leftarrow S[i] + \mathcal{L}_t(X_t^{(i)})$ 
11    $i^* = \arg \min_i S[i]$  // Best scored latent
12    $I_0 \leftarrow \mathcal{D}(X_0^{(i^*)})$  // Decode to pixel space

```

Table 11. Latent selection on IntraCompBench. With the base models [7, 43], best-of-10 selection is applied with ISAC.

Method	Multi-Class Accuracy (\uparrow)					Multi-Instance Accuracy (\uparrow)					Efficiency (\downarrow)	
	#2	#3	#4	#5	Avg.	#2	#3	#4	#5	Avg.	Latency	VRAM
Flux.1-dev [7]	84%	37%	3%	2%	31%	97%	89%	82%	66%	83%	50s	37.2GB
+ ISAC _{LS} (Ours)	97%	48%	38%	19%	51%	99%	94%	85%	72%	88%	85s	40.8GB
Qwen-Image [43]	91%	45%	33%	10%	48%	98%	92%	84%	70%	86%	140s	60.1GB
+ ISAC _{LS} (Ours)	99%	58%	42%	25%	56%	99%	96%	89%	78%	91%	210s	65.3GB

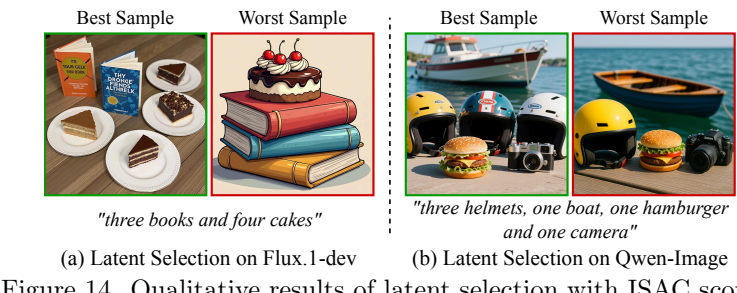


Figure 14. Qualitative results of latent selection with ISAC scoring.

Table 12. Extension of ISAC to fine-tuned models [51, 63], evaluated on IntraCompBench.

Method	Multi-Class Accuracy (\uparrow)					Multi-Instance Accuracy (\uparrow)					Efficiency (\downarrow)	
	#2	#3	#4	#5	Avg.	#2	#3	#4	#5	Avg.	Latency	VRAM
TokenCompose _{SD1.4} [51]	27%	4%	1%	0%	8%	77%	65%	41%	13%	49%	12s	8.5GB
+ ISAC (Ours)	62%	36%	28%	17%	36%	84%	80%	60%	30%	63%	33s	17.9GB
IterComp _{SDXL} [63]	11%	5%	4%	0%	5%	95%	73%	64%	37%	67%	49s	11.8GB
+ ISAC (Ours)	46%	28%	26%	21%	30%	99%	93%	85%	55%	83%	100s	29.9GB

Table 13. Performance-aesthetic trade-off on SDXL. “Class” and “Instance” are multi-class and multi-instance accuracy, respectively.

Method	Class (\uparrow)	Instance (\uparrow)	FID (\downarrow)	CMMD (\downarrow)
SDXL [4]	7%	61%	0.0000	0.0000
+ A&E [10]	14%	62%	13.802	0.0018
+ ISAC (Ours)	34%	76%	16.402	0.0026

C.2 Integration with Fine-tuned Models

To demonstrate ISAC’s complementarity, we apply it atop two fine-tuning methods that enhance spatial understanding via external supervision: TokenCompose [51] and IterComp [63]. TokenCompose [51] fine-tunes cross-attention alignment using segmentation masks from Grounded SAM [62], while IterComp [63] uses iterative preference-guided refinement leveraging RPG [30] and InstanceDiffusion [25]. As shown in Tab. 12, adding ISAC further improves both multi-class and multi-instance accuracy for both methods. Note that TokenCompose [51] uses `float32` weights, increasing latency and VRAM compared to standard SD1.4 [1].

C.3 Effect of ISAC on Image Quality

To make the quality–accuracy trade-off explicit, we provide Frechet Inception Distance (FID) [64] and CLIP [65]-based Maximum Mean Discrepancy (CMMD) [66] evaluations alongside the compositional metrics in Tab. 13. All images are generated from the T2I-CompBench [13] Numeracy task. We adopt FID as a standard image-quality metric and CMMD as a complementary measure, as it evaluates distributional distances in CLIP [65] embedding space—commonly used by recent aesthetic evaluation models (*e.g.*, ImageReward [67]). FID and CMMD are measured between each method’s output distribution and the native SDXL [4] distribution; a lower value therefore indicates less deviation from the native SDXL aesthetic.

ISAC significantly boosts multi-class accuracy by +27 %p and multi-instance accuracy by +15 %p over baseline SDXL—more than twice the gain of A&E [10]. Despite these large compositional improvements, ISAC maintains excellent visual fidelity, as evidenced by its competitive FID (16.4) and CMMD (0.0026), which remain close to those of A&E [10]. This confirms ISAC’s ability to substantially enhance compositional accuracy without introducing notable visual artifacts.

C.4 Performance Stability of ISAC

It is known that an initial random seed (X_T) significantly impact the compositional image generation performance [68]. To see its impact, we report the stability of base models and

ISAC across initial random seeds in Tab. 16. As IntraCompBench already consider the seed variance by generating 10 images from a single prompt and 10 different seeds, we measured the variance with T2I-CompBench [13] Numeracy task. Importantly, ISAC reduces standard deviation by approximately 3–4 times, clearly demonstrating ISAC’s consistent improvement across diverse prompts and initializations. Fig. 22 qualitatively shows this stability as well.

C.5 Limitation

ISAC currently lacks an explicit understanding of 3D space, which leads to a notable failure mode. Figure 15 illustrates one such example: correctly positioning objects that are being viewed through transparent materials requires 3D-aware reasoning. In future work, we plan to explore extensions of ISAC with 3D- or physics-aware guidance.

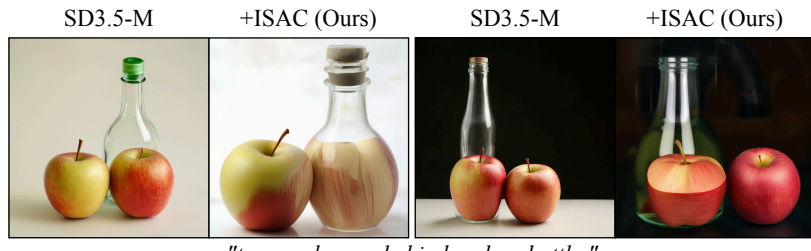


Figure 15. Limitation of ISAC.

Appendix D. Future Works

Most of ISAC’s additional computational cost comes from applying backpropagation through *all* attention layers in the diffusion model. A natural way to reduce this overhead is to identify informative attention layers and apply backpropagation only to those. Ahn et al. [69] explore such informative layers and empirically find that specific attention layers in the mid-block of the U-Net [46] are particularly important for guidance. Figure 16 and Table 14 show that ISAC exhibits a similar trend, suggesting that layer-wise selection is a promising direction for improving ISAC’s efficiency.

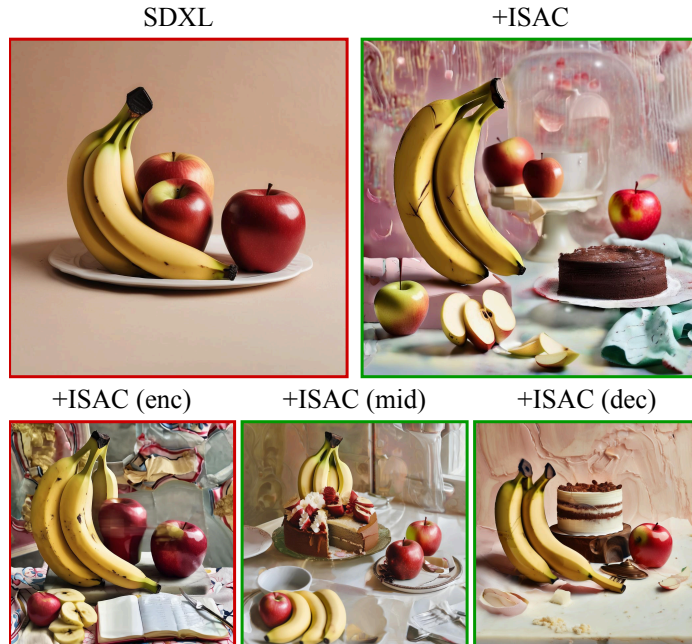


Figure 16. ISAC applied to different subsets of SDXL [4] attention layers.

Table 14. Complexity analysis of SDXL [4] and ISAC variants.

Method	Latency (s) (↓)	VRAM (GB) (↓)
SDXL [4] w/o attention	10.7	18.0
+ ISAC	111.4	30.7
+ ISAC (enc)	60.9	<u>21.2</u>
+ ISAC (mid)	<u>31.7</u>	18.0
+ ISAC (dec)	60.4	25.0

Appendix E. Additional Diffusion Dynamics Visualization

In Fig. 17, we show the extended visualization of Fig. 4 to popular diffusion models [1, 5] and ISAC’s dynamics on SD3.5-M [5]. The two-step instance formation and instance-centric semantic separation achieves highly reliable multi-object generation.

Appendix F. Additional Quantitative Results

We provide full quantitative results on IntraCompBench metrics in Table 15. The results are obtained by applying ISAC to various models, including SD1.4, SD1.5, SD2.1 [1], SDXL [4], SD3.5-M, SD3.5-L [5], PixArt- α [6], PixArt- Σ [47] and Flux.1-dev [7].

Also in Tab. 16, we provide extended quantitative results of ISAC on IntraCompBench and public counting benchmark T2I-CompBench [13], where prompts specify exact counts. It is worth note that SD1.5 [1] with ISAC surpasses baseline performance of plain SDXL [4] and ISAC reduces performance variance from initial seeds (see Sec. C for details).

Appendix G. Additional Qualitative Results

Generality beyond simple prompts Figure 18,19 and 20 show additional qualitative comparisons of ISAC with other attention control methods, InitNO [2], Self-Cross [3]. The results show that ISAC not only improves drawing multiple instances, but also improves assigning correct attributes to each instance. Beyond simple color attributes, ISAC is also effective to shape, texture, positioning and the combination of them. This highlights ISAC’s broader applicability.

Robust multi-instance generation across seeds We provide qualitative results when generating 5 images with a fixed prompt, “*three cats*”, on SD1.5 [1] and SD3.5-M [5]. When the baseline output already contains the correct number of instances, ISAC minimally alters the result. However, when the baseline produces too few or too many instances, ISAC effectively corrects the output (see Figs. 22a and 22b). These results show that ISAC reliably helps correct instance counts across diverse seeds for a fixed prompt, while leaving correct samples mostly unchanged.

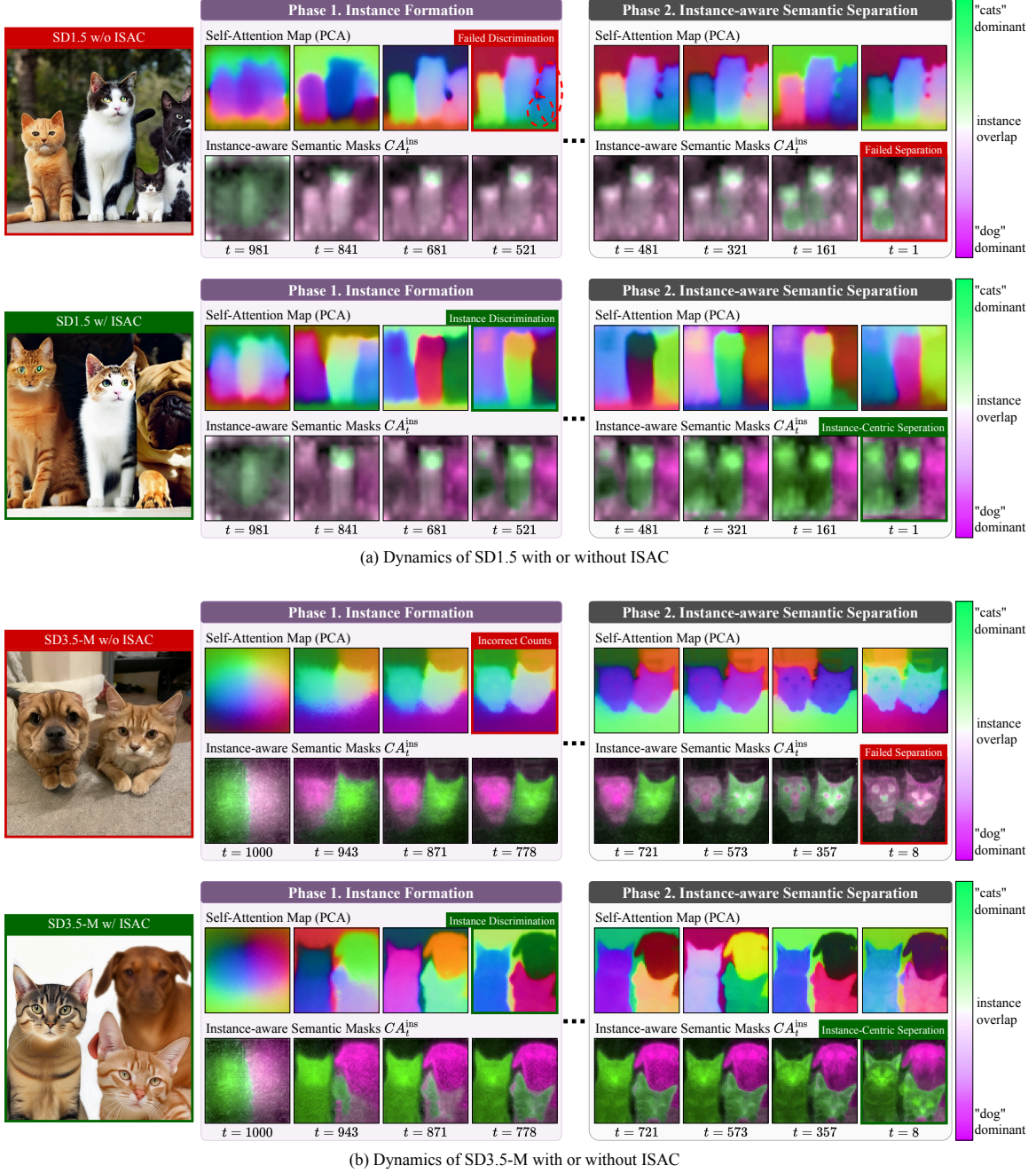


Figure 17. **Diffusion dynamics visualization with or without ISAC.** This is an extended version of Fig. 4 to SD1.5 [1] and SD3.5-M [5].

Table 15. Additional quantitative results of latent optimization methods on IntraCompBench.

Method	Multi-Class Accuracy (\uparrow)					Multi-Instance Accuracy (\uparrow)					Efficiency (\downarrow)	
	#2	#3	#4	#5	Avg.	#2	#3	#4	#5	Avg.	Latency	VRAM
SD1.4 [1]	30%	2%	1%	0%	8%	94%	74%	28%	22%	55%	8s	4.9GB
+ A&E SIGGRAPH'23 [10]	50%	9%	8%	2%	17%	97%	79%	26%	23%	56%	17s	9.2GB
+ SynGen NeurIPS'23 [17]	54%	11%	6%	2%	18%	90%	69%	25%	19%	51%	19s	9.3GB
+ InitNO CVPR'24 [2]	58%	10%	7%	4%	20%	94%	79%	31%	20%	56%	20s	9.6GB
+ TEBOpt NeurIPS'24 [9]	55%	13%	8%	2%	19%	91%	73%	31%	20%	54%	17s	9.3GB
+ ISAC (Ours)	66%	34%	29%	16%	36%	100%	90%	51%	40%	70%	21s	9.7GB
SD1.5 [1]	28%	2%	1%	0%	8%	88%	65%	36%	26%	54%	12s	4.4 GB
+ A&E SIGGRAPH'23 [10]	48%	10%	5%	2%	16%	91%	68%	34%	24%	54%	24s	9.1 GB
+ SynGen NeurIPS'23 [17]	50%	9%	4%	2%	16%	84%	61%	38%	22%	51%	27s	9.2 GB
+ InitNO CVPR'24 [2]	55%	12%	7%	5%	20%	90%	68%	40%	29%	57%	29s	9.5 GB
+ Self-Cross CVPR'25 [3]	48%	8%	4%	2%	15%	89%	67%	38%	27%	55%	21s	10 GB
+ TEBOpt NeurIPS'24 [9]	52%	11%	8%	3%	18%	87%	65%	36%	27%	54%	25s	9.2 GB
+ ISAC (Ours)	65%	31%	29%	18%	36%	95%	82%	56%	44%	69%	30s	9.6 GB
SD2.1 [1]	31%	6%	3%	0%	10%	91%	74%	41%	28%	58%	13s	4.8 GB
+ A&E SIGGRAPH'23 [10]	53%	12%	4%	1%	18%	94%	79%	39%	29%	60%	26s	9.3 GB
+ SynGen NeurIPS'23 [17]	55%	10%	7%	3%	19%	87%	69%	38%	25%	55%	29s	9.4 GB
+ InitNO CVPR'24 [2]	59%	13%	11%	5%	22%	91%	79%	44%	26%	60%	31s	9.7 GB
+ TEBOpt NeurIPS'24 [9]	56%	14%	7%	6%	21%	88%	75%	44%	27%	58%	27s	9.4 GB
+ ISAC (Ours)	67%	35%	34%	20%	39%	98%	88%	64%	42%	73%	32s	9.8 GB
SDXL [4]	20%	4%	3%	0%	7%	90%	71%	49%	32%	61%	48s	12.8 GB
+ ISAC (Ours)	57%	32%	29%	17%	34%	96%	89%	71%	47%	76%	101s	29.8 GB
PixArt- α [6]	27%	3%	1%	0%	8%	99%	93%	33%	15%	60%	17s	19.9 GB
+ ISAC (Ours)	63%	30%	29%	21%	36%	100%	100%	56%	31%	72%	40s	53.7 GB
PixArt- Σ [47]	39%	8%	0%	0%	12%	98%	98%	30%	16%	60%	18s	19.9 GB
+ ISAC (Ours)	78%	39%	31%	20%	42%	100%	100%	48%	31%	70%	41s	53.8 GB
SD3.5-M [5]	62%	23%	12%	3%	25%	84%	71%	51%	51%	64%	40s	22.9 GB
+ A&E SIGGRAPH'23 [10]	65%	29%	16%	5%	28%	86%	72%	52%	50%	65%	124s	73.8 GB
+ SynGen NeurIPS'23 [17]	66%	28%	15%	6%	28%	82%	68%	50%	48%	62%	131s	74.3 GB
+ InitNO CVPR'24 [2]	77%	31%	17%	7%	33%	84%	73%	52%	49%	65%	138s	74.6 GB
+ Self-Cross CVPR'25 [3]	78%	38%	19%	3%	34%	86%	72%	51%	50%	65%	147s	76.4 GB
+ TEBOpt NeurIPS'24 [9]	78%	31%	19%	8%	34%	85%	71%	52%	52%	65%	139s	74.5 GB
+ ISAC (Ours)	98%	51%	40%	20%	52%	98%	91%	72%	69%	83%	140s	74.8 GB

Table 16. Quantitative results on T2I-CompBench [13] Numeracy and IntraCompBench multi-instance tasks. Performance stability across initial random seeds is measured on T2I-CompBench, with 30 seeds. **Bold** shows the best and underline shows the second best performance.

Method	# Parameters	T2I-CompBench	IntraCompBench (Multi-Instance) (\uparrow)					
			Numeracy (\uparrow)	#2	#3	#4	#5	Avg.
SD1.5 [1]	0.8B	$46.5\% \pm 5.1\%$	88%	65%	36%	26%	54%	
+ ISAC (Ours)	<u>0.8B</u>	<u>$55.0\% \pm 1.4\%$</u>	<u>95%</u>	<u>82%</u>	<u>56%</u>	<u>44%</u>	<u>69%</u>	
SDXL [4]	2.6B	$51.1\% \pm 4.8\%$	90%	71%	49%	32%	61%	
+ ISAC (Ours)	<u>2.6B</u>	<u>$64.0\% \pm 1.2\%$</u>	<u>96%</u>	<u>89%</u>	<u>71%</u>	<u>47%</u>	<u>76%</u>	

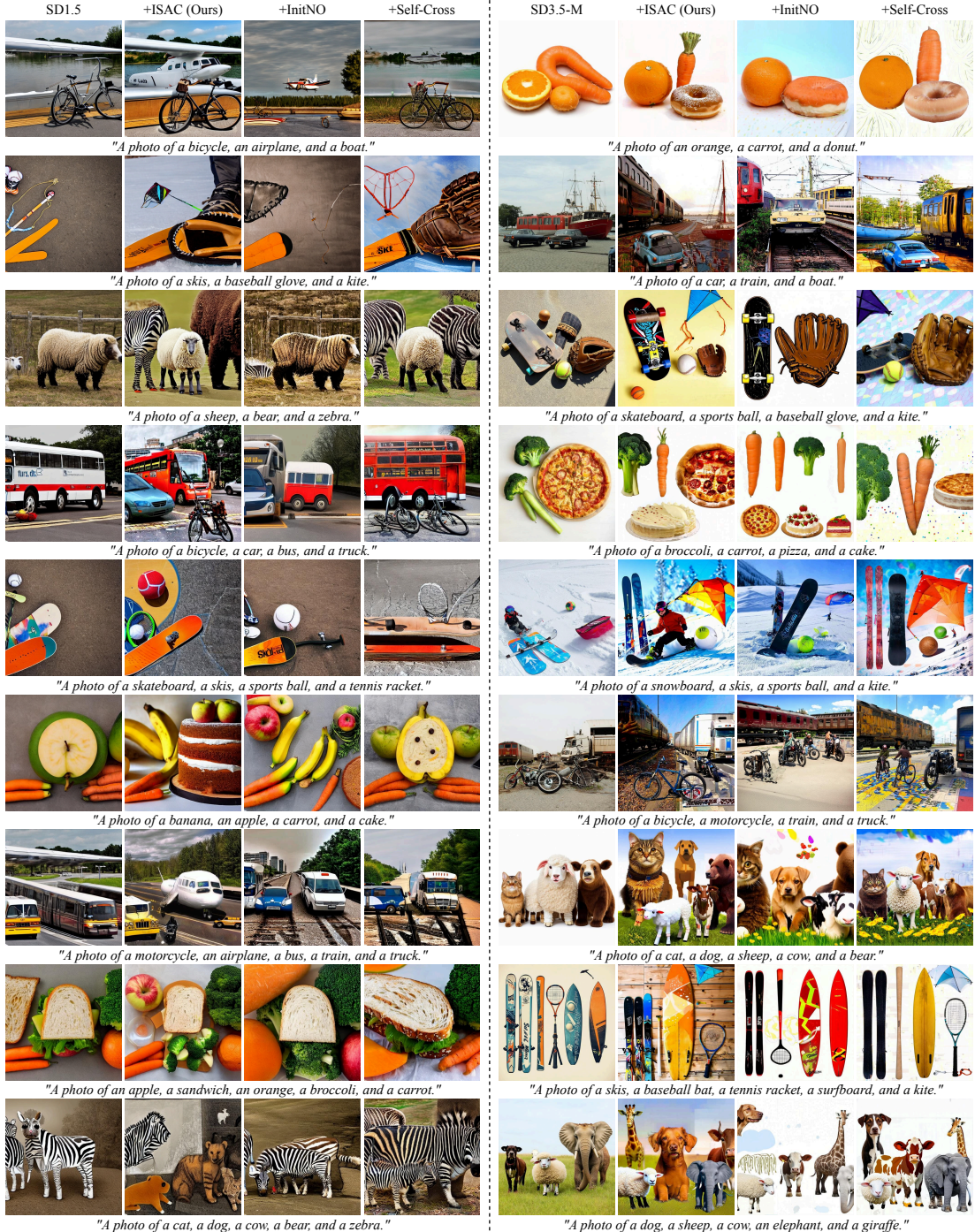


Figure 18. Qualitative comparisons of attention control methods, InitNO [2], Self-Cross [3] and ISAC, in 3 to 5 intra-category generation. All prompts are drawn from IntraCompBench.

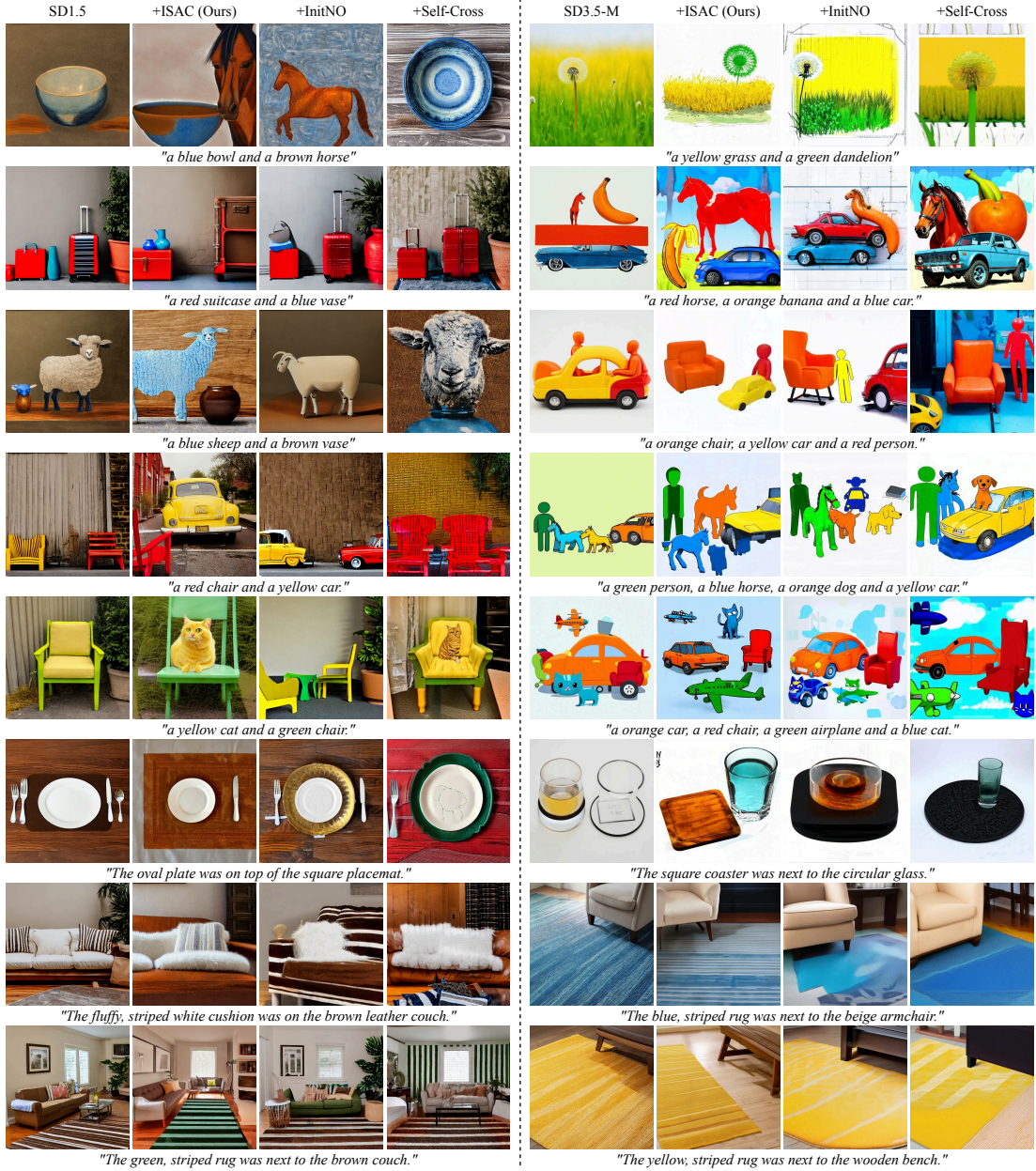


Figure 19. Qualitative comparisons of attention control methods, InitNO [2], Self-Cross [3] and ISAC, in complex scene generation. It requires the model to correctly bind attributes such as color, texture, spatial, and shape. All prompts are drawn from HRS-Bench [14] and T2I-CompBench [13].

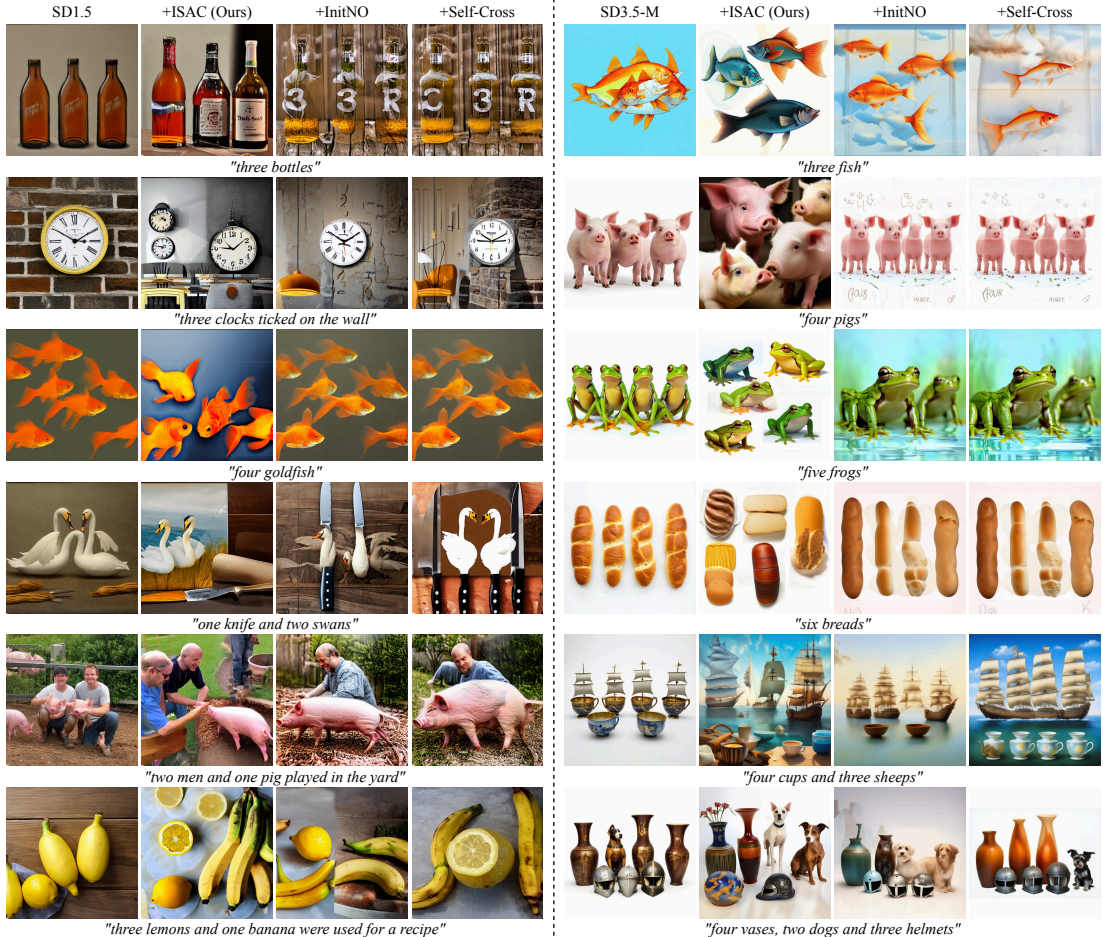


Figure 20. Qualitative comparisons of attention control methods, InitNO [2], Self-Cross [3] and ISAC, in general multi-instance scenarios. It requires the model to correctly generate multiple instances from one or more classes. All prompts are drawn from T2I-CompBench [13] Numeracy task.

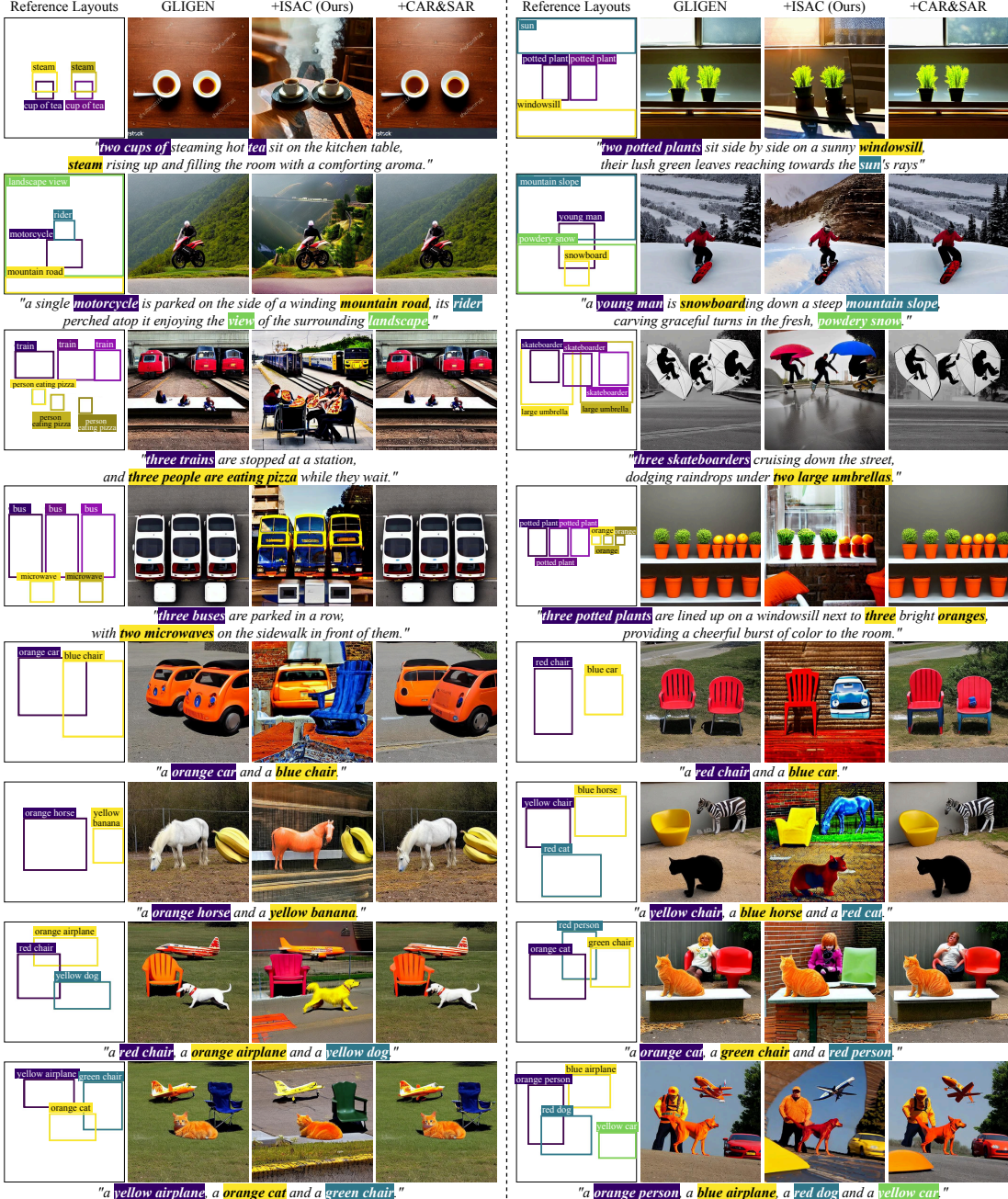
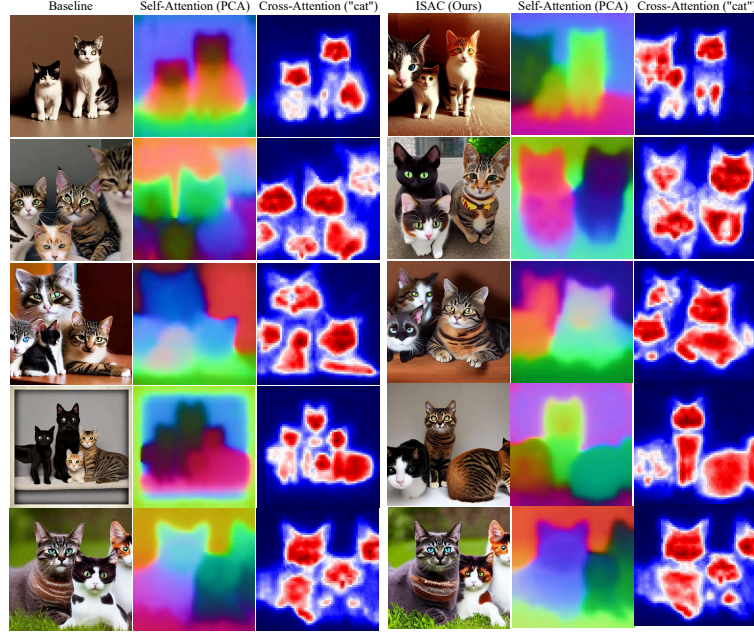
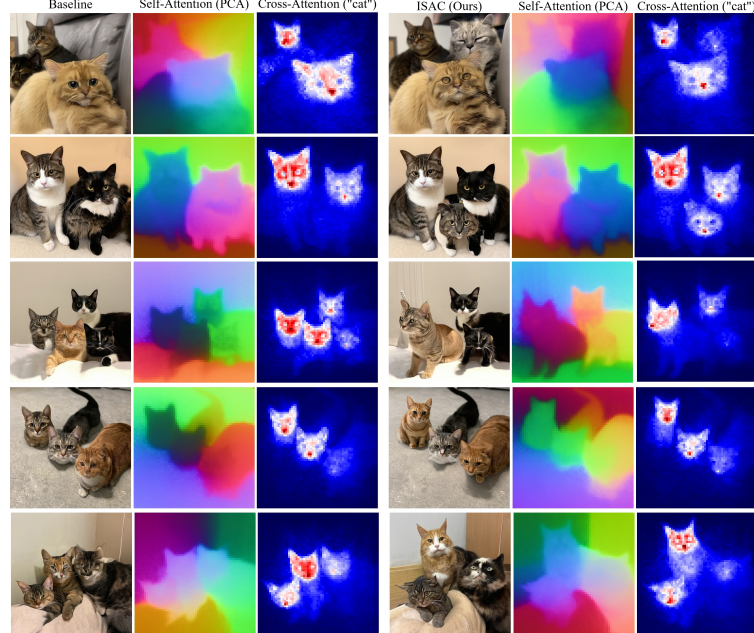


Figure 21. Qualitative comparisons of ISAC with layout guidance method, Attention Refocusing (CAR&SAR) [37] on top of finetuned layout model GLIGEN [12]. All prompts are drawn from HRS-Bench [13].



(a) Result from Stable Diffusion v1.5 [1].



(b) Result from Stable Diffusion v3.5-M [5].

Figure 22. Qualitative results across multiple seeds for the prompt “*three cats*”, which involves multiple instances of the same class. Our method (right) consistently generates images with the correct instance count, sharper object boundaries, and improved separation compared to the baseline (left).

References

- [1] R. Rombach, A. Blattmann, D. Lorenz, P. Esser, and B. Ommer, “High-resolution image synthesis with latent diffusion models,” in *Proceedings of the IEEE/CVF conference on computer vision and pattern recognition*, pp. 10684–10695, 2022.
- [2] X. Guo, J. Liu, M. Cui, J. Li, H. Yang, and D. Huang, “Initno: Boosting text-to-image diffusion models via initial noise optimization,” in *CVPR*, 2024.
- [3] W. Qiu, J. Wang, and M. Tang, “Self-cross diffusion guidance for text-to-image synthesis of similar subjects,” in *Proceedings of the Computer Vision and Pattern Recognition Conference*, pp. 23528–23538, 2025.
- [4] D. Podell, Z. English, K. Lacey, A. Blattmann, T. Dockhorn, J. Müller, J. Penna, and R. Rombach, “Sdxl: Improving latent diffusion models for high-resolution image synthesis,” *arXiv preprint arXiv:2307.01952*, 2023.
- [5] P. Esser, S. Kulal, A. Blattmann, R. Entezari, J. Müller, H. Saini, Y. Levi, D. Lorenz, A. Sauer, F. Boesel, *et al.*, “Scaling rectified flow transformers for high-resolution image synthesis,” in *Forty-first international conference on machine learning*, 2024.
- [6] J. Chen, J. Yu, C. Ge, L. Yao, E. Xie, Y. Wu, Z. Wang, J. Kwok, P. Luo, H. Lu, and Z. Li, “Pixart- α : Fast training of diffusion transformer for photorealistic text-to-image synthesis,” 2023.
- [7] B. F. Labs, “Flux.” <https://github.com/black-forest-labs/flux>, 2024.
- [8] T. Hu, L. Li, J. van de Weijer, H. Gao, F. Shahbaz Khan, J. Yang, M.-M. Cheng, K. Wang, and Y. Wang, “Token merging for training-free semantic binding in text-to-image synthesis,” *Advances in Neural Information Processing Systems*, vol. 37, pp. 137646–137672, 2024.
- [9] C.-Y. Chen, C. Tseng, L.-W. Tsao, and H.-H. Shuai, “A cat is a cat (not a dog!): Unraveling information mix-ups in text-to-image encoders through causal analysis and embedding optimization,” *Advances in Neural Information Processing Systems*, 2024.
- [10] H. Chefer, Y. Alaluf, Y. Vinker, L. Wolf, and D. Cohen-Or, “Attend-and-excite: Attention-based semantic guidance for text-to-image diffusion models,” 2023.
- [11] S. Jo, Z. Lee, W. Lee, and K. Kim, “Diffegg: Diffusion-driven edge generation as a pixel-annotation-free alternative for instance annotation,” 2025.
- [12] Y. Li, H. Liu, Q. Wu, F. Mu, J. Yang, J. Gao, C. Li, and Y. J. Lee, “Gligen: Open-set grounded text-to-image generation,” *CVPR*, 2023.
- [13] K. Huang, C. Duan, K. Sun, E. Xie, Z. Li, and X. Liu, “T2i-compbench++: An enhanced and comprehensive benchmark for compositional text-to-image generation,” *IEEE Transactions on Pattern Analysis and Machine Intelligence*, vol. 47, no. 5, pp. 3563–3579, 2025.
- [14] E. M. Bakr, P. Sun, X. Shen, F. F. Khan, L. E. Li, and M. Elhoseiny, “Hrs-bench: Holistic, reliable and scalable benchmark for text-to-image models,” in *Proceedings of the IEEE/CVF International Conference on Computer Vision*, pp. 20041–20053, 2023.
- [15] L. Binyamin, Y. Tewel, H. Segev, E. Hirsch, R. Rassin, and G. Chechik, “Make it count: Text-to-image generation with an accurate number of objects,” *arXiv preprint arXiv:2406.10210*, 2024.
- [16] W. Kang, K. Galim, H. I. Koo, and N. I. Cho, “Counting guidance for high fidelity text-to-image synthesis,” in *2025 IEEE/CVF Winter Conference on Applications of Computer Vision (WACV)*, pp. 899–908, IEEE, 2025.
- [17] R. Rassin, E. Hirsch, D. Glickman, S. Ravfogel, Y. Goldberg, and G. Chechik, “Linguistic binding in diffusion models: Enhancing attribute correspondence through attention map alignment,” *Advances in Neural Information Processing Systems*, vol. 36, 2024.
- [18] T. H. S. Meral, E. Simsar, F. Tombari, and P. Yanardag, “Conform: Contrast is all you need for high-fidelity text-to-image diffusion models,” in *Proceedings of the IEEE/CVF Conference on Computer Vision and Pattern Recognition*, pp. 9005–9014, 2024.

- [19] S. Liu, Z. Zeng, T. Ren, F. Li, H. Zhang, J. Yang, Q. Jiang, C. Li, J. Yang, H. Su, *et al.*, “Grounding dino: Marrying dino with grounded pre-training for open-set object detection,” in *European Conference on Computer Vision*, pp. 38–55, Springer, 2024.
- [20] A. Hertz, R. Mokady, J. Tenenbaum, K. Aberman, Y. Pritch, and D. Cohen-Or, “Prompt-to-prompt image editing with cross attention control,” *arXiv preprint arXiv:2208.01626*, 2022.
- [21] W. Feng, X. He, T.-J. Fu, V. Jampani, A. R. Akula, P. Narayana, S. Basu, X. E. Wang, and W. Y. Wang, “Training-free structured diffusion guidance for compositional text-to-image synthesis,” in *The Eleventh International Conference on Learning Representations*, 2023.
- [22] L. Lian, B. Li, A. Yala, and T. Darrell, “Llm-grounded diffusion: Enhancing prompt understanding of text-to-image diffusion models with large language models,” *arXiv preprint arXiv:2305.13655*, 2023.
- [23] X. Zhang, L. Yang, Y. Cai, Z. Yu, K. Wang, J. Xie, Y. Tian, M. Xu, Y. Tang, Y. Yang, and B. Cui, “Realcompo: Balancing realism and compositionality improves text-to-image diffusion models,” *Advances in Neural Information Processing Systems*, 2024.
- [24] D. Zhou, Y. Li, F. Ma, X. Zhang, and Y. Yang, “Mige: Multi-instance generation controller for text-to-image synthesis,” in *Proceedings of the IEEE/CVF Conference on Computer Vision and Pattern Recognition*, pp. 6818–6828, 2024.
- [25] X. Wang, T. Darrell, S. S. Rambhatla, R. Girdhar, and I. Misra, “Instancediffusion: Instance-level control for image generation,” 2024.
- [26] B. Cheng, Y. Ma, L. Wu, S. Liu, A. Ma, X. Wu, D. Leng, and Y. Yin, “Hico: Hierarchical controllable diffusion model for layout-to-image generation,” 2024.
- [27] D. Zhou, J. Xie, Z. Yang, and Y. Yang, “3dis: Depth-driven decoupled instance synthesis for text-to-image generation,” *arXiv preprint arXiv:2410.12669*, 2024.
- [28] H. Zhang, D. Hong, Y. Wang, J. Shao, X. Wu, Z. Wu, and Y.-G. Jiang, “Creatilayout: Siamese multimodal diffusion transformer for creative layout-to-image generation,” in *Proceedings of the IEEE/CVF International Conference on Computer Vision*, pp. 18487–18497, 2025.
- [29] B. Li, C.-Y. Wang, H. Xu, X. Zhang, E. Armand, D. Srivastava, S. Xiaojun, Z. Chen, J. Xie, and Z. Tu, “Overlaybench: A benchmark for layout-to-image generation with dense overlaps,” in *Proceedings of the 39th Conference on Neural Information Processing Systems (NeurIPS 2025), Datasets and Benchmarks Track*, Neural Information Processing Systems Foundation, 2025.
- [30] L. Yang, Z. Yu, C. Meng, M. Xu, S. Ermon, and B. Cui, “Mastering text-to-image diffusion: Recaptioning, planning, and generating with multimodal llms,” in *International Conference on Machine Learning*, 2024.
- [31] O. Bar-Tal, L. Yariv, Y. Lipman, and T. Dekel, “Multidiffusion: Fusing diffusion paths for controlled image generation,” *arXiv preprint arXiv:2302.08113*, 2023.
- [32] T. Shirakawa and S. Uchida, “Noisecollage: A layout-aware text-to-image diffusion model based on noise cropping and merging,” in *Proceedings of the IEEE/CVF Conference on Computer Vision and Pattern Recognition*, 2024.
- [33] J. Xie, Y. Li, Y. Huang, H. Liu, W. Zhang, Y. Zheng, and M. Z. Shou, “Boxdiff: Text-to-image synthesis with training-free box-constrained diffusion,” in *Proceedings of the IEEE/CVF International Conference on Computer Vision (ICCV)*, pp. 7452–7461, 2023.
- [34] M. Chen, I. Laina, and A. Vedaldi, “Training-free layout control with cross-attention guidance,” *arXiv preprint arXiv:2304.03373*, 2023.
- [35] J. Xiao, L. Li, H. Lv, S. Wang, and Q. Huang, “R&b: Region and boundary aware zero-shot grounded text-to-image generation,” 2023.
- [36] P. Y. Lee, T. Yoon, and M. Sung, “Groundit: Grounding diffusion transformers via noisy patch transplantation,” in *Advances in Neural Information Processing Systems*, 2024.
- [37] Q. Phung, S. Ge, and J.-B. Huang, “Grounded text-to-image synthesis with attention refocusing,” in *Proceedings of the IEEE/CVF Conference on Computer Vision and Pattern Recognition*, pp. 7932–7942, 2024.

[38] O. Dahary, O. Patashnik, K. Aberman, and D. Cohen-Or, “Be yourself: Bounded attention for multi-subject text-to-image generation,” 2024.

[39] O. Dahary, Y. Cohen, O. Patashnik, K. Aberman, and D. Cohen-Or, “Be decisive: Noise-induced layouts for multi-subject generation,” in *Proceedings of the Special Interest Group on Computer Graphics and Interactive Techniques Conference Conference Papers*, pp. 1–12, 2025.

[40] Y. Hu, B. Liu, J. Kasai, Y. Wang, M. Ostendorf, R. Krishna, and N. A. Smith, “Tifa: Accurate and interpretable text-to-image faithfulness evaluation with question answering,” in *Proceedings of the IEEE/CVF International Conference on Computer Vision*, pp. 20406–20417, 2023.

[41] H. Lee, H. Lee, S. Gye, and J. Kim, “Beta sampling is all you need: Efficient image generation strategy for diffusion models using stepwise spectral analysis,” in *2025 IEEE/CVF Winter Conference on Applications of Computer Vision (WACV)*, pp. 4215–4224, IEEE, 2025.

[42] A. Wang, L. Liu, H. Chen, Z. Lin, J. Han, and G. Ding, “Yoloe: Real-time seeing anything,” 2025.

[43] C. Wu, J. Li, J. Zhou, J. Lin, K. Gao, K. Yan, S. ming Yin, S. Bai, X. Xu, Y. Chen, Y. Chen, Z. Tang, Z. Zhang, Z. Wang, A. Yang, B. Yu, C. Cheng, D. Liu, D. Li, H. Zhang, H. Meng, H. Wei, J. Ni, K. Chen, K. Cao, L. Peng, L. Qu, M. Wu, P. Wang, S. Yu, T. Wen, W. Feng, X. Xu, Y. Wang, Y. Zhang, Y. Zhu, Y. Wu, Y. Cai, and Z. Liu, “Qwen-image technical report,” 2025.

[44] OpenAI, “gpt-oss-120b & gpt-oss-20b model card,” 2025.

[45] M. Hobley and V. Prisacariu, “Learning to count anything: Reference-less class-agnostic counting with weak supervision,” *arXiv preprint arXiv:2205.10203*, 2022.

[46] O. Ronneberger, P. Fischer, and T. Brox, “U-net: Convolutional networks for biomedical image segmentation,” in *International Conference on Medical image computing and computer-assisted intervention*, pp. 234–241, Springer, 2015.

[47] J. Chen, C. Ge, E. Xie, Y. Wu, L. Yao, X. Ren, Z. Wang, P. Luo, H. Lu, and Z. Li, “Pixart- σ : Weak-to-strong training of diffusion transformer for 4k text-to-image generation,” in *European Conference on Computer Vision*, pp. 74–91, Springer, 2024.

[48] D. Comaniciu and P. Meer, “Mean shift: A robust approach toward feature space analysis,” *IEEE Transactions on pattern analysis and machine intelligence*, vol. 24, no. 5, pp. 603–619, 2002.

[49] J.-J. Hwang, S. X. Yu, J. Shi, M. D. Collins, T.-J. Yang, X. Zhang, and L.-C. Chen, “Segsort: Segmentation by discriminative sorting of segments,” in *Proceedings of the IEEE/CVF international conference on computer vision*, pp. 7334–7344, 2019.

[50] R. Liu, J. Lehman, P. Molino, F. Petroski Such, E. Frank, A. Sergeev, and J. Yosinski, “An intriguing failing of convolutional neural networks and the coordconv solution,” *Advances in neural information processing systems*, vol. 31, 2018.

[51] Z. Wang, Z. Sha, Z. Ding, Y. Wang, and Z. Tu, “Tokencompose: Text-to-image diffusion with token-level supervision,” in *Proceedings of the IEEE/CVF Conference on Computer Vision and Pattern Recognition (CVPR)*, pp. 8553–8564, June 2024.

[52] T.-Y. Lin, M. Maire, S. Belongie, J. Hays, P. Perona, D. Ramanan, P. Dollár, and C. L. Zitnick, “Microsoft COCO: Common objects in context,” in *ECCV*, pp. 740–755, Springer, 2014.

[53] Y. Tian, Q. Ye, and D. Doermann, “Yolov12: Attention-centric real-time object detectors,” *arXiv preprint arXiv:2502.12524*, 2025.

[54] D. Shen, G. Song, Z. Xue, F.-Y. Wang, and Y. Liu, “Rethinking the spatial inconsistency in classifier-free diffusion guidance,” in *Proceedings of the IEEE/CVF Conference on Computer Vision and Pattern Recognition*, pp. 9370–9379, 2024.

[55] J. Ho and T. Salimans, “Classifier-free diffusion guidance,” *arXiv preprint arXiv:2207.12598*, 2022.

[56] Z. Wang, D. Peng, F. Chen, Y. Yang, and Y. Lei, “Training-free dense-aligned diffusion guidance for modular conditional image synthesis,” in *Proceedings of the Computer Vision and Pattern Recognition Conference*, pp. 13135–13145, 2025.

- [57] A. Bansal, H.-M. Chu, A. Schwarzschild, S. Sengupta, M. Goldblum, J. Geiping, and T. Goldstein, “Universal guidance for diffusion models,” in *Proceedings of the IEEE/CVF Conference on Computer Vision and Pattern Recognition*, pp. 843–852, 2023.
- [58] K. Kim and J. C. Ye, “Noise2score: tweedie’s approach to self-supervised image denoising without clean images,” *Advances in Neural Information Processing Systems*, vol. 34, pp. 864–874, 2021.
- [59] Y. Lipman, R. T. Chen, H. Ben-Hamu, M. Nickel, and M. Le, “Flow matching for generative modeling,” *arXiv preprint arXiv:2210.02747*, 2022.
- [60] D. Park, S. Kim, T. Moon, M. Kim, K. Lee, and J. Cho, “Rare-to-frequent: Unlocking compositional generation power of diffusion models on rare concepts with llm guidance,” *The Thirteenth International Conference on Learning Representations*, 2025.
- [61] D. Jiang, G. Song, X. Wu, R. Zhang, D. Shen, Z. Zong, Y. Liu, and H. Li, “Comat: Aligning text-to-image diffusion model with image-to-text concept matching,” *arXiv preprint arXiv:2404.03653*, 2024.
- [62] T. Ren, S. Liu, A. Zeng, J. Lin, K. Li, H. Cao, J. Chen, X. Huang, Y. Chen, F. Yan, *et al.*, “Grounded sam: Assembling open-world models for diverse visual tasks,” *arXiv preprint arXiv:2401.14159*, 2024.
- [63] X. Zhang, L. Yang, G. Li, Y. Cai, J. Xie, Y. Tang, Y. Yang, M. Wang, and B. Cui, “Itercomp: Iterative composition-aware feedback learning from model gallery for text-to-image generation,” *arXiv preprint arXiv:2410.07171*, 2024.
- [64] M. Heusel, H. Ramsauer, T. Unterthiner, B. Nessler, and S. Hochreiter, “Gans trained by a two time-scale update rule converge to a local nash equilibrium,” *Advances in neural information processing systems*, vol. 30, 2017.
- [65] A. Radford, J. W. Kim, C. Hallacy, A. Ramesh, G. Goh, S. Agarwal, G. Sastry, A. Askell, P. Mishkin, J. Clark, *et al.*, “Learning transferable visual models from natural language supervision,” in *International conference on machine learning*, pp. 8748–8763, PMLR, 2021.
- [66] S. Jayasumana, S. Ramalingam, A. Veit, D. Glasner, A. Chakrabarti, and S. Kumar, “Rethinking fid: Towards a better evaluation metric for image generation,” in *Proceedings of the IEEE/CVF Conference on Computer Vision and Pattern Recognition*, pp. 9307–9315, 2024.
- [67] J. Xu, X. Liu, Y. Wu, Y. Tong, Q. Li, M. Ding, J. Tang, and Y. Dong, “Imagereward: Learning and evaluating human preferences for text-to-image generation,” *Advances in Neural Information Processing Systems*, vol. 36, pp. 15903–15935, 2023.
- [68] S. Li, H. Le, J. Xu, and M. Salzmann, “All seeds are not equal: Enhancing compositional text-to-image generation with reliable random seeds,” *arXiv preprint arXiv:2411.18810*, 2024.
- [69] D. Ahn, H. Cho, J. Min, W. Jang, J. Kim, S. Kim, H. H. Park, K. H. Jin, and S. Kim, “Self-rectifying diffusion sampling with perturbed-attention guidance,” in *European Conference on Computer Vision*, pp. 1–17, Springer, 2024.